

MASTER'S THESIS

---

**Optical trapping of micron-sized objects  
to search for new physics beyond the  
Standard Model**

---

*Thesis by:*  
Chang-ling LI

*Under the supervision of:*  
Pr. David C. MOORE  
Physics Department  
Yale University

*A thesis submitted in partial fulfillment of the requirements for the degrees of*  
**Diplôme d'ingénieur de l'Ecole CentraleSupélec**  
*and*  
**Master Nanophysique de l'Université Paris-Saclay**

June-September 2019



# Contents

<b>Introduction</b>	<b>1</b>
<b>1 Brief theory of single-beam optical tweezers</b>	<b>3</b>
1.1 Qualitative description of single-beam optical trap . . . . .	3
1.2 Equation of motion of a trapped sphere . . . . .	4
1.3 Necessity of a feedback cooling system . . . . .	5
<b>2 Experimental setup</b>	<b>9</b>
2.1 Trapping and imaging systems . . . . .	9
2.2 Feedback system . . . . .	11
2.3 Sources of electrical noise and backgrounds . . . . .	11
<b>3 Sensitivity and pre-chamber</b>	<b>13</b>
3.1 Motivations for a pre-chamber . . . . .	13
3.1.1 Spectral analysis . . . . .	13
3.1.2 Laser pointing noise . . . . .	14
3.2 Pre-chamber: design and manufacturing . . . . .	19
3.2.1 Design of the pre-chamber . . . . .	19
3.2.2 Connection to the main chamber and sealing . . . . .	20
3.2.3 Pre-chamber manufacturing . . . . .	23
<b>4 Mass attractor for short-range gravity measurements</b>	<b>25</b>
4.1 Introduction . . . . .	25
4.2 Discussion on the design of the mass attractor . . . . .	26
4.3 Principle of the experiment . . . . .	26
4.4 Experimental Methods . . . . .	29
4.4.1 Droplets generator . . . . .	29
4.4.2 Heavy Liquid . . . . .	29
4.4.3 Detection system . . . . .	30
4.4.4 Capillary Holder . . . . .	31
4.4.5 Preliminary tests . . . . .	33
4.4.6 Flow generation system improvement . . . . .	34
4.4.7 Preliminary background tests inside the vacuum chamber . . . . .	35
<b>A PID Feedback system</b>	<b>37</b>
<b>B Spectral Analysis</b>	<b>39</b>
<b>C Calculation of the Yukawa potential for this experiment</b>	<b>41</b>



# List of Abbreviations

<b>AOM</b>	<b>Acousto-Optic Modulator</b>
<b>BPD</b>	<b>Balanced PhotoDiode</b>
<b>CAM</b>	<b>CAMera</b>
<b>DAQ</b>	<b>Data AcQuisition (system)</b>
<b>DOF(s)</b>	<b>Degree(s) Of Freedom</b>
<b>FPGA</b>	<b>Field Programmable Gate Array</b>
<b>ID</b>	<b>Internal Diameter</b>
<b>NA</b>	<b>Numerical Aperture</b>
<b>PID</b>	<b>Proportional Integral Proportional (controller)</b>
<b>PSD</b>	<b>Power Spectral Density</b>
<b>OD</b>	<b>Outer Diameter</b>
<b>QPD</b>	<b>Quadrant PhotoDiode</b>



# Introduction

In the attempt to build a unified and consistent theory of the physical world, the Standard Model of particle physics has up to now been highly predictive describing the known particles and three of the known fundamental interactions - the electromagnetic, the strong and the weak nuclear interactions [1]. The gravitational interaction, although studied and experimentally tested long before the other interactions, remains the only one which reveals theoretical inconsistencies that prevent its quantum description [2]. Theories beyond the Standard Model have been developed in the recent decades to coherently give a microscopic description of gravity, or to address the nature of the dark matter and dark energy that pervade the universe. Some of these theories imply deviations of the Newtonian inverse-square law at length scales below  $\sim 1\text{mm}$  [3]–[7]. Deviations from the Newtonian potential can be parameterized by an additional Yukawa-like potential as follows:

$$V = -\frac{Gm_1m_2}{r}(1 + \alpha e^{-\frac{r}{\lambda}}) \quad (1)$$

where  $\alpha$  represents the relative strength of the Yukawa interaction compared to the Newtonian one, at a characteristic length scale  $\lambda$  [8]. Many experiments have tested Yukawa-like potentials at length scales ranging from atomic [9] to cosmological [10], [11]. Figure 1 shows the parameter space where these tests have already excluded a Yukawa-type deviation. As shown, the most severe constraints have been set on cosmological length scales, while sub-millimetre length scales still remain to be explored [12].

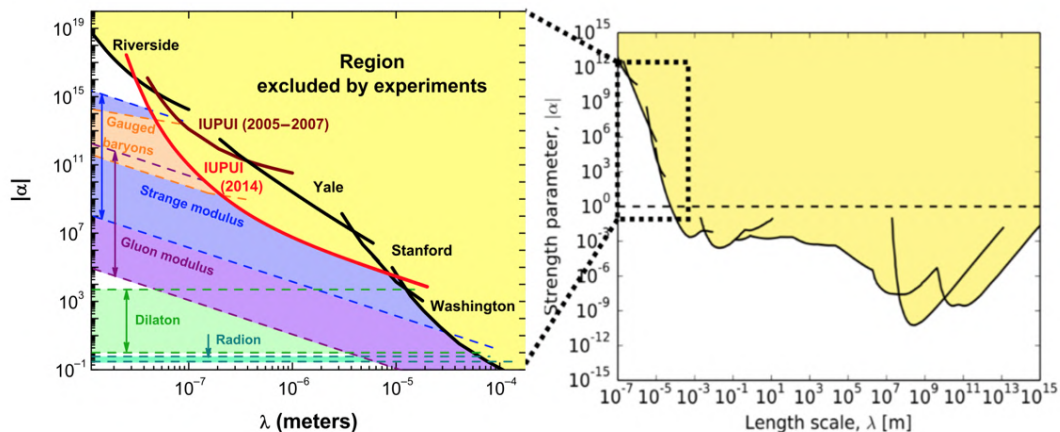


FIGURE 1: Parameter space experimentally excluded in the search for Yukawa-type non-Newtonian gravitational potentials [12], [13] The left picture focuses on the sub-millimetre length scales where tests of gravity still remain to be explored.

Tests of gravity become more problematic at small length scales because of the relative weakness of gravitational interactions compared with other sources of noise

as well as backgrounds. This implies that high measurement sensitivity is necessary for them to be detected. Noise, such as thermal noise or noise from electronic devices, includes all kinds of omnipresent random processes affecting measurements and which can be averaged out over long measurement times but also reduced if sources of noise are found and properly monitored. On the other hand, backgrounds such as electrical interactions between a charged test mass and its environment are associated to real signals which always add to the signal of interest and must be distinguished from it. In tests of gravity, Earth's gravitational field also represents a source of significant background : considering two centimetre size test masses, the gravitational force acting between them is found to be eight orders of magnitude smaller than their respective weight. This is the reason why in order to eliminate this first-order background, test masses are generally suspended (see for example Cavendish's experiment [14]). While many experiments currently employ mechanical suspension as for example with torsion balances [15], micro-cantilevers [16] or micro-oscillators [13], these techniques engage intrinsic second-order backgrounds and noise due to mechanical, electrical or thermal couplings with the suspension mechanism.

The advent of the laser in the middle of the XXth century has enabled optical levitation and control of small objets – typically between 100nm and  $30\mu m$  – with light [17]. These optical tweezers follow the pioneering works of Ashkin who first achieved stable levitation of micron-sized spheres in the late 1960s [18]–[21]. Contrary to mechanical suspension, stable optical levitation provides mechanical isolation, while thermal noise and electrical backgrounds can be improved, for instance by working in high vacuum in the case of thermal noise. This can thus enable considerable improvements regarding the attainable sensitivities and favours optical levitation as a way to test gravity below  $\sim 50\mu m$ , where measurements have not yet reached enough sensitivity to measure gravitational interaction between such small masses [12].

In the following experiment, optical trapping of micron-sized dielectric spheres is used to build highly sensitive force sensors and test up-to-now unexplored short-range gravitational interactions.

## Chapter 1

# Brief theory of single-beam optical tweezers

### 1.1 Qualitative description of single-beam optical trap

Optical forces are omnipresent: as photons beam carry momentum, conservation of momentum implies that a light beam scattered from an object exerts a force on it. However, optical forces are generally too weak to be perceptible and even highly focused intense laser beams can only be used to levitate small objects - typically between  $100nm$  and  $30\mu m$  [17]. Following Ashkin's works cited in the introduction, many applications emerged, ranging from experiments in biology where viruses and bacteria could be manipulated [22]–[24] to the building of precision sensors for fundamental physics experiments [25]–[27]. Three optical trap configurations are mainly used. The first and most simple trapping configuration uses a single beam propagating upwards to counter-balance the weight of the sphere [28]. Single-beam traps with high enough numerical aperture can also trap objects without relying on their counter-balancing weight [29]. Eventually, it is possible to use two counter propagating beams [17]. The following description will limit to single-beam optical traps counter-balancing gravity.

When the characteristic size  $R$  of the levitated object is bigger than the wavelength  $\lambda_0$  of the light, which is the case in this experiment where spheres with diameters in  $[5 - 30\mu m]$  are levitated using  $1064\text{ nm}$  laser beams, one may use the ray optics approximation to quantify the optical forces acting on it [17]. Silica spheres used in this experiment have a typical refractive index  $n_{sph} = 1.46$  different from the refractive index of the air ( $n_{air} = 1$ ). If a light ray impinges the sphere, it is partly reflected and partly transmitted in directions following Snell-Descartes' laws:

$$\theta_i = \theta_r \quad (1.1)$$

$$n_{air}\sin\theta_i = n_{sph}\sin\theta_t \quad (1.2)$$

where  $\theta_i$  is the angle of incidence,  $\theta_r$  the angle of the reflected beam and  $\theta_t$  the angle of the transmitted beam.

The ratio between the transmitted and reflected powers can be derived from Maxwell's equations with appropriate continuity conditions at the surface of the sphere. Qualitatively, as the direction of the total momentum of the reflected and transmitted light does not equal the momentum of the incoming beam, a transfer of momentum from the incoming beam to the sphere occurs, resulting in a net force acting on the sphere. Ashkin derived for each ray of the beam the theoretical expression of this net force, split into a *scattering force*  $\vec{F}_s$  parallel to the direction of

propagation of the beam and a *gradient force*  $\vec{F}_g$  perpendicular to it [30]. If  $R$  and  $T$  are Fresnel's reflection and transmission coefficients respectively:

$$F_s = \frac{n_{air}P}{c} \left\{ 1 + R(\cos 2\theta_i) - T^2 \frac{\cos(2\theta_i - 2\theta_t) + R \cos(2\theta_i)}{1 + R^2 + 2R \cos(2\theta_t)} \right\} \quad (1.3)$$

$$F_g = \frac{n_{air}P}{c} \left\{ R \sin(2\theta_i) - T^2 \frac{\sin(2\theta_i - 2\theta_t) + R \sin(2\theta_i)}{1 + R^2 + 2R \cos(2\theta_t)} \right\} \quad (1.4)$$

Neglecting at first the contribution of the reflected light at the surface of the sphere ( $\sim 5\%$  of the incoming power), one can qualitatively predict an equilibrium position of the sphere slightly above the focal point of the beam. Figure 1.1 shows cases where the sphere is deviated from an initial position set slightly above the focal point of a beam (a) in the radial (b) and axial (c and d) directions. In the case of a radial drift, an increasing deflection of the transmitted beam in the direction of the drift implies a counter force in the opposite direction, restoring the sphere to its initial position. If the sphere goes up, i.e. further away from the more intense focal point of the beam, the intensity of the transmitted light is reduced, resulting in a smaller upward force pushing down the sphere to its initial position. In the same way, if the sphere goes down closer to the more intense focal point of the beam, the more intense transmitted beam enhances the upward force which pushes the sphere up to its initial position.

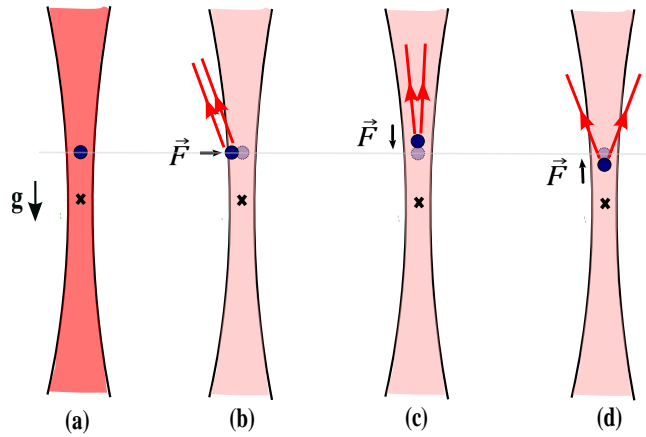


FIGURE 1.1: Qualitative view of the stability of an optical trap. The dark cross gives the position of the focal point of the beam while the dotted gray line is the initial position of the sphere. From its initial position (a), a sphere drifting slightly in the radial (b) or axial (c and d) directions experiences a restoring forces which pushes it back to its initial position.

Using symmetry arguments and Taylor expansion, the optical trap can therefore be approximated by a three-dimensional harmonic potential for small displacements around its equilibrium position.

## 1.2 Equation of motion of a trapped sphere

A free particle suspended in a fluid at thermal equilibrium presents a random motion due to collisions with the surrounding fast-moving molecules of the fluid. This motion, discovered by Robert Brown in 1827 and consequently named after him

Brownian motion, can be described by the Langevin equation in each direction of space [31]:

$$M \frac{d^2x}{dt^2} + \gamma \frac{dx}{dt} = F_{therm}(t) \quad (1.5)$$

where  $M$  is the mass of the suspended particle within the fluid. In the second term standing for the frictional force exerted by the fluid with viscosity  $\eta$  on the particle,  $\gamma$  is the frictional coefficient which is given by the Stokes coefficient for a spherical particle with radius  $R$ :  $\gamma = 6\pi\eta R$ . The random nature of the Brownian motion is modelled by a stochastic force  $F_{therm}(t)$  which expression at a given room temperature  $T$  is given by:

$$F_{therm}(t) = (2k_B T \gamma)^{1/2} \zeta(t) \quad (1.6)$$

where  $k_B$  is Boltzmann's constant and  $\zeta(t)$  a normalized white-noise process verifying (the averages are taken over all times  $t$  and  $t'$ ):

$$\langle \zeta(t) \rangle = 0 \quad \text{and} \quad \langle \zeta(t) \zeta(t') \rangle = \delta(t - t') \quad (1.7)$$

An optically trapped microsphere in air can be seen as such a suspended particle, although not free but inside a potential which can be approximated by a harmonic potential for small displacements. In this case, the Langevin equation for this system can thus be rewritten in each direction of space as follows:

$$\frac{d^2x}{dt^2} + \Gamma_0 \frac{dx}{dt} + \omega_0^2 x = \Lambda \zeta(t) \quad (1.8)$$

where  $\Gamma_0 = \gamma/M$  is the air viscous damping coefficient,  $\Lambda = (2k_B T \gamma)^{1/2}/M$  and if  $\kappa$  is the stiffness of the trap,  $\omega_0 = \sqrt{\kappa/M}$  represents the resonance frequency of the sphere for an undamped harmonic oscillator.

The equation of motion of the sphere appears as the equation of a noisy damped harmonic oscillator for which at a given temperature, the stochastic term on the right side is proportional to  $\Lambda \propto \sqrt{\gamma} \propto \sqrt{\eta}$ . Therefore and as mentioned in the introduction, in order to reduce the thermal noise associated to the Brownian nature of the motion of the sphere and hence increase measurements sensitivity to the sphere's acceleration, one must work at low pressures. The following experiment is performed using a vacuum chamber which pressure can be lowered down to  $\lesssim 10^{-7}$  mbar.

### 1.3 Necessity of a feedback cooling system

Equation 1.8 shows that air viscosity  $\eta$  simultaneously appears in the noise and damping terms: air molecules which create fluctuations on the motion of the sphere also dissipate its energy (fluctuation-dissipation theorem). This means that by decreasing the room pressure while maintaining the same temperature, air-induced fluctuations should always be balanced by air damping, keeping the center of mass of the sphere at a constant temperature. As the depth of the trapping laser remains constant when the pressure is lowered, the sphere should *a priori* be stable at low pressures.

Experimental observations show however that spheres stably trapped in vacuum are lost within few seconds past a given transition pressure [32]. In this experiment,

a  $15.0 \pm 2.7 \mu\text{m}$  sphere stably trapped at 1mbar becomes unstable and leaves the trap when the pressure is pumped down below  $\sim 0.1\text{mbar}$ .

In order to go down to high vacuum to reduce noise and thus increase sensitivity, a feedback system is necessary to stabilize the microsphere within the trap. One possibility is to apply an additional damping force on the sphere in each direction of space and with the following form:

$$F^{cool} = -\Gamma^{cool} \frac{dx}{dt} \quad (1.9)$$

Equation 1.8 therefore becomes:

$$\frac{d^2x}{dt^2} + (\Gamma_0 + \Gamma^{cool}) \frac{dx}{dt} + \omega_0^2 x = \Lambda \zeta(t) \quad (1.10)$$

One notices that contrary to the damping from the air which is also contained in the stochastic heating term,  $F^{cool}$  only has a cooling effect on the motion of the sphere. Such a feedback cooling is also called “cold damping” [33]. This damping can be achieved using the derivative part of a proportional-integral-derivative (PID) feedback cooling system, described in Appendix A.

Figure 1.2 was obtained by acquiring the time stream of the sphere’s position in the radial direction when the feedback system is alternatively turned on and off following a square-wave trigger. When the feedback is turned off, the sphere rapidly gains energy and fluctuates around its equilibrium position. If the frequency of the triggering square-wave was reduced, the sphere would acquire enough energy to jump out of the optical trap.

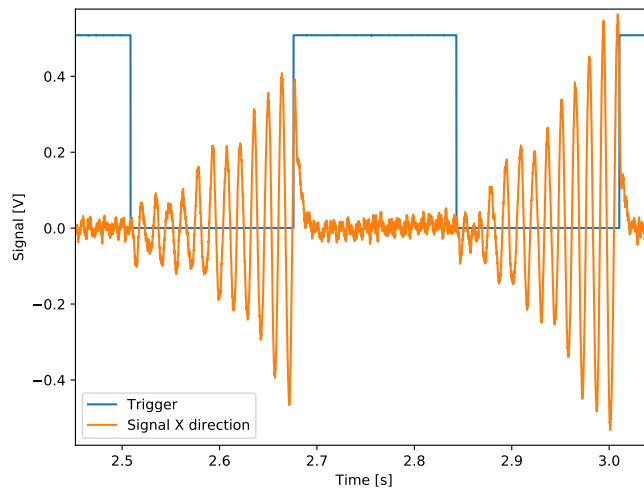


FIGURE 1.2: (orange) Time stream of a  $15.0 \pm 2.7 \mu\text{m}$  sphere’s position in one of the two radial directions at  $< 10^{-6}\text{mbar}$  when the feedback system is alternatively turned on and off following a square-wave trigger (blue). The heating rate measured was found to be  $\Gamma/2\pi \sim 3\text{Hz}$ , more than six orders of magnitude above the theoretical value of  $\Gamma_0 \sim 10^{-6}\text{Hz}$  at this pressure.

It is possible to derive the theoretical values of the damping coefficient  $\Gamma_0$  and draw its evolution with pressure [33]. Figure 1.3 shows in plain lines and for approximate monoatomic gas compositions the expected values of  $\Gamma_0$  at pressures below  $10^2\text{ mbar}$ . The dark dotted line is the measured value of the heating coefficient

for a  $15.0 \pm 2.7 \mu\text{m}$  sphere at  $10^{-6}$  mbar, showing a six orders of magnitude difference with the theoretical value at this pressure. If we assume that this high heating value is associated with a pressure-independent noise signal, the crossing point with the theoretical curve would give a transition pressure. The existence of a transition pressure for which the trap becomes unstable means that Equation 1.8 does not fully describe the motion of the sphere at low pressures.

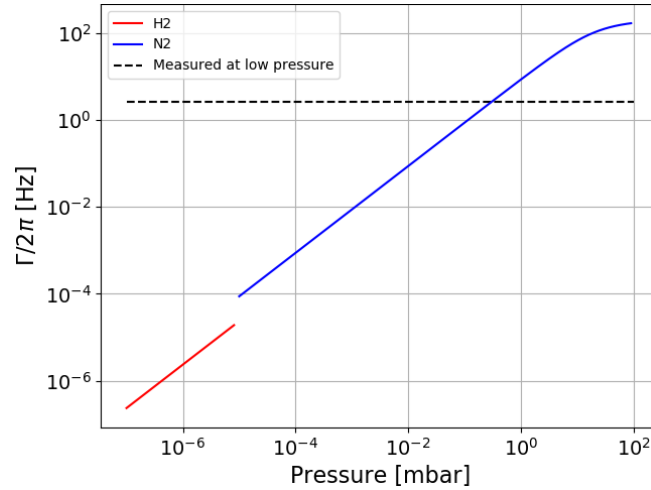


FIGURE 1.3: Theoretical values of the damping coefficient  $\Gamma_0$  for a system following Equation 1.8 and their evolution with pressure. Molecular composition of the air is approximated to the most realistic monoatomic gas at a given pressure. The dotted line is the experimentally observed value of the heating coefficient for a  $15.0 \pm 2.7 \mu\text{m}$  sphere at  $10^{-6}$  mbar. A transition pressure is observed slightly above 0.1 mbar, for which the trap is observed to become unstable

Indeed, the trapping laser does not only provide a stabilizing optical harmonic potential but also a source of heating for the sphere as well as additional sources of noise. While heating may originate from absorption processes or the non-conservative nature of the scattering optical force [33], additional sources include laser amplitude and pointing noise, i.e. power and displacement fluctuations of the trapping laser beam, respectively [34].

Considering a noisy heating term  $\Theta(t)$ , the final equation of motion of a trapped sphere when the feedback is turned on can be written as:

$$\frac{d^2x}{dt^2} + (\Gamma_0 + \Gamma^{cool}) \frac{dx}{dt} + \omega_0^2 x = \Lambda \zeta(t) + \Theta(t) \quad (1.11)$$

This last heating term  $\Theta(t)$  represents a source of noise which affects the current sensitivity of this experiment at first order. In the following chapter, we review hypotheses and tests proposed to account for the possible causes producing  $\Theta(t)$ , with the aim of eventually minimizing it.



## Chapter 2

# Experimental setup

As discussed in the previous sections, this experiment aims at using optically levitated spheres as highly sensitive sensors to *in fine* measure gravitational interactions at micron-size scales. Therefore, the main concerns when designing the experimental setup relate to the anticipation and reduction of possible sources of noise and backgrounds that could affect the measurements. In the following section, we describe the general setup of the experiment and the different technical choices adopted to minimize noise and backgrounds.

### 2.1 Trapping and imaging systems

We saw in Chapter 1 that the most simple optical trap is formed by a single vertically oriented beam counteracting the weight of a given test mass, while the study of the equation of motion of a trapped sphere concluded that a low pressure environment is needed to reduce thermal noise. In this experiment, silica microspheres with diameters ranging from  $\sim 15\mu\text{m}$  to  $\sim 23\mu\text{m}$  are trapped slightly above the focal point of a vertically oriented 1064 nm laser beam. The trapping area is confined in a vacuum chamber which pressure can be lowered down to  $\sim 10^{-7}$  mbar.

The trapping system is shown on the simplified schematic of the experimental setup in Figure 2.1. The trapping beam is formed at the input of the chamber, represented by regions 1 and 2. Setups for both regions are physically confined in two distinct spaces and region 2 will be of special interest in the following Chapter 3.

In order to image the three-dimensional motion of the sphere, two additional 532 nm laser beams are used: one is co-aligned with the trapping beam to image the radial components of the sphere's motion (XY plane) while the second one, orthogonal to the first one, is centred at the height of the trapping position to image the vertical position of the sphere (Z-axis). The Z-imaging beam has a waist much larger than the size of the sphere to provide a full image of its surroundings.

At the output of the vacuum chamber, the trapping beam is dumped after a harmonic beam splitter while both imaging beams are used to form two microscope images of the levitated sphere using two CCD cameras (CAM). Figure 2.2 shows images of a  $22\mu\text{m}$  sphere in both (XZ) and (XY) planes, respectively.

The rest of the imaging beams is used to get the associated position time streams for all three degrees of freedom (DOFs) of the sphere. The beam imaging the X-Y horizontal plane is split in half to get position signals in X and Y directions separately. For both directions, a D-shaped mirror splits the beams in half again while a balanced photodiode (BPD) collects the two half-split signals. The final signal is amplified and sent to a data acquisition system (DAQ). A similar acquisition system is used for the Z-imaging beam.

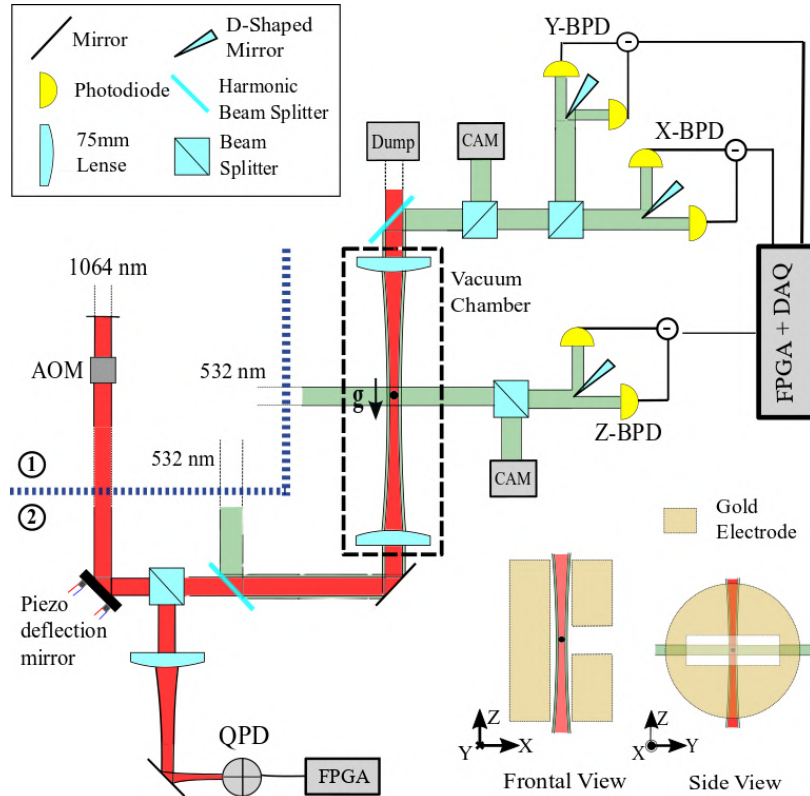


FIGURE 2.1: Simplified schematic of the setup. A sphere is trapped using a 1064 nm beam with numerical aperture  $NA \approx 0.02$  propagating upward in the Z direction. Regions 1 and 2 gather the input optical setup that forms the 1064 nm trapping beam and the two 532 nm beams which image the three-dimensional position of the sphere. One of the imaging beams is co-aligned with the trapping beam to image the radial degrees of freedom (DOFs) of the sphere. The second imaging beam, orthogonal to the first one and with a larger waist, is centred at the height of the trapping position to image the vertical position of the sphere. At the output of the vacuum chamber, the trapping beam is dumped while images of the sphere's three-dimensional position are recorded using two CCD cameras (CAM). For all three DOFs X, Y and Z, the imaging light transmitted past the sphere is also used to measure the position time stream using a D-shaped mirror and a balanced photodiode (BPD) connected to a data acquisition system (DAQ). These position time streams are then used as input signals of the feedback system, performed using a field-programmable gate array (FPGA). The vertical position of the sphere is fed back by modulating the power of the trapping laser through an acousto-optic modulator (AOM) positioned before the chamber, while the FPGA controls the radial position of the sphere by controlling the displacement DOFs of the trapping beam through the two angular DOFs of a piezo deflection mirror. A quadrant photodiode (QPD) is also placed before the chamber and at the same focal distance as the trapping position to provide the pointing position of the trapping laser (XY plane) as well as delivering feedback on it through both the AOM and piezo deflection mirror. Frontal and side views display the presence of two gold electrodes in the vicinity of the sphere, one of which with a hole at the center to let room for the mass attractor to approach the sphere.

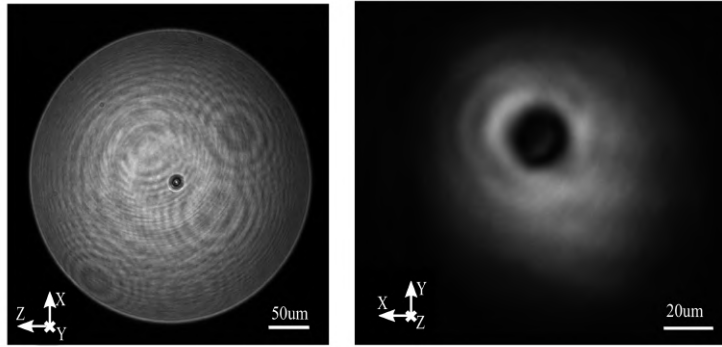


FIGURE 2.2: Images of a  $\sim 23\mu\text{m}$  trapped sphere recorded by the two CCD cameras at the output of the vacuum chamber. (left) Image of the vertical X-Z plane transmitted from the Z-imaging beam. (right) Image of the horizontal X-Y plane transmitted from the X-Y imaging beam. The relative large waist of the Z-imaging beam explains the difference in scale between both images.

## 2.2 Feedback system

Chapter 1 showed that a feedback loop is required below a transition pressure for which heating effects surpass the damping from air and cause the sphere to gain enough energy to leave the trap. Here, imaging signals which provide microscope images of the levitated sphere are also acquired as position time streams for all three DOFs and sent as input signals of a feedback system acting on the trapping beam.

Output signals from the BPDs are fed into a field-programmable gate array (FPGA) as input signals for a feedback loop. The FPGA applies a feedback on the vertical position of the sphere by adjusting the power of the trapping beam with an acousto-optic modulator (AOM, region 1) while the feedback on the X and Y degrees of freedom is permitted by controlling the displacement DOFs of the trapping beam by modulating the two angular DOFs of a piezo deflection mirror (region 2).

Another feedback loop can be implemented before the vacuum chamber to reduce the amplitude and pointing noise of the trapping laser beam. In order to do that, a quadrant photodiode (QPD) is placed before the chamber using a lens with same focal distance as the trapping position to provide the pointing position of the trapping laser. Also connected to the FPGA, it therefore provides the input signal of the pointing position of the trapping laser to be fed back through both modulations of the AOM and piezo deflection mirror.

## 2.3 Sources of electrical noise and backgrounds

Although using a vacuum chamber with active feedback at low pressures allows considerable thermal noise reduction, other sources of noise, especially electrical ones, may appear and must therefore be considered in the design of the experimental setup.

Because of the method used to load spheres into the trap, described in detail in [25], a trapped sphere never comes perfectly neutral but generally presents extra negative charges that can be estimated to reach few thousands of  $e^-$ . Residual charges as well as AC currents and fields present inside the chamber would thus exert Coulomb forces on the sphere, far exceeding the gravitational forces we want to measure [8]. This electrical noise would affect the motion of the sphere and thus be

recorded by the DAQ. One way to reduce electrical noise consists in discharging the sphere to a zero net charge. In this setup, the light of a UV-lamp is flashed onto the location of the sphere to discharge it using the photoelectric effect [25], [32]. As shown in the frontal and side views of Figure 2.1, the trapping location is caught between two gold electrodes. A known and tuneable electric field up to a few kV/cm can be applied between them. Therefore, the residual extra charge of the sphere after each flash can be evaluated relatively by observing the response motion of the sphere. When the charge of the sphere becomes smaller than  $\sim 10e^-$ , increasing the field between the electrodes reveals discrete steps corresponding to individual charges. A null charge is reached when the motion response of the sphere becomes negligible even when applying high voltages.<sup>1</sup> A detailed description of the discharging process is available in [25]. Even when fully discharged though, the permanent and induced dipoles of the sphere couple with the surrounding noisy electric field and represent a second-order source of electrical noise that affects measurements sensitivity [35]. The projection of the permanent dipole moment orthogonal to the spinning axis of the sphere can be averaged out by monitoring the rotation of the sphere [36].

For this experiment, one of the electrodes has a hole in the center to allow room for the mass attractor which is described in Chapter 4.

---

<sup>1</sup>This means that for a  $\sim 15\mu\text{m}$  silica sphere with mass density  $\rho_{\text{SiO}_2} = 1.8\text{g}/\text{cm}^3$ , it is possible to resolve 1 excess net charge out of  $> 10^{14}$  charges that a sphere contains.

## Chapter 3

# Sensitivity and pre-chamber

### 3.1 Motivations for a pre-chamber

We saw in section 1.3 that a sphere trapped using the previously described experimental setup becomes unstable at low pressures, where a first-order noisy heating effect must be counter-balanced by a feedback cooling system in order for the sphere not to be lost. In the following section, we review observations which led to speculate on the physical origin of this noise.

#### 3.1.1 Spectral analysis

Equation 1.11 describing the motion of a trapped sphere with a feedback turned on can be rewritten in the frequency domain:

$$\hat{x}(\omega) = \frac{\Lambda_{\zeta}^{\hat{}}(\omega) + \hat{\Theta}(\omega)}{\omega_0^2 - \omega^2 - i\omega(\Gamma_0 + \Gamma_j^{cool})} \quad (3.1)$$

where  $\Lambda_{\zeta}^{\hat{}}(\omega)$  is the Fourier transform of the stochastic force and  $\hat{\Theta}(\omega)$  the Fourier transform of the additional noisy heating force exerted on the sphere by the trapping laser. If the time stream is acquired during  $T_{acq}$ , the associated expression of the power spectral density (PSD, see definition in Appendix B) is given by:

$$S_{xx}(\omega) = \frac{|\hat{x}(\omega)|^2}{T_{acq}} = \frac{1}{T_{acq}} \frac{|\Lambda_{\zeta}^{\hat{}}(\omega) + \hat{\Theta}(\omega)|^2}{(\omega_0^2 - \omega^2)^2 + \omega_0^2(\Gamma_0 + \Gamma_j^{cool})^2} \quad (3.2)$$

Figure 3.1 shows the amplitude spectra  $\sqrt{S_{xx}(\omega)}$  of signals from the balanced photodiode in the X direction (X-BPD, see Figure 2.1) in different conditions. The blue spectrum is drawn when a sphere is trapped at high pressure  $\sim 1\text{mbar}$  with no feedback. The curves below (green, red, purple, brown and orange respectively) are associated to the motion of a trapped sphere at low pressure  $\sim 10^{-6}\text{mbar}$  when the feedback loop is turned on with increasing gain values. These spectra show a high response around 100Hz, corresponding to the sphere centre of mass's resonance frequency and clearly damped by the feedback system. The peak at 60Hz translates the power-line frequency in the United States.

Because a damped harmonic potential acts as a low-pass filter, a sphere trapped in this potential will mostly respond to excitations below its resonance frequency. Therefore, the frequency range below  $\sim 100\text{Hz}$  appears as the relevant frequency range where future short-range gravity experiments will be performed, hence where high sensitivity is sought. For this reason, the feedback system has been designed to be frequency-tuneable (see Appendix A). More specifically as observed in the spectra at low pressure, for small gains it weakly affects the frequency range of interest

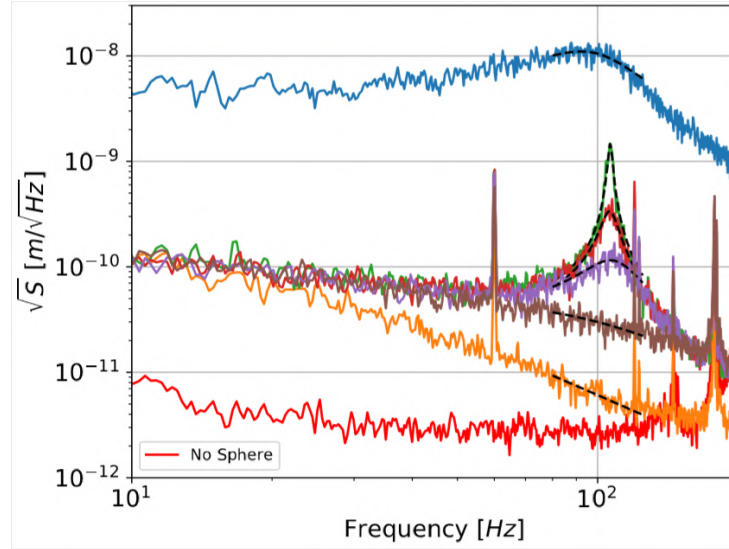


FIGURE 3.1: Amplitude spectra of a trapped sphere's X DOF, calculated from a time stream recorded by the X-BPD in different conditions. The blue curve, corresponding to a sphere trapped at  $\sim 1\text{mbar}$ , presents a white noise component two orders of magnitude above the green, dark red, purple, brown and orange spectra which are drawn at  $\sim 10^{-6}\text{mbar}$  with increasing gain values applied for the feedback system, respectively. A resonance frequency at  $\sim 100\text{Hz}$  is clearly visible. The red bottom curve is obtained when there is no sphere in the trap, thus standing for the noise associated to the imaging system. The spectra at low pressure display a white noise component  $\sim$  one order of magnitude above the expected value showed by the red bottom curve.

below  $\sim 70\text{Hz}$ :  $\Gamma^{cool}(f = \omega/2\pi < 70\text{Hz}) \sim 0$ . Indeed, although an efficient feedback loop in the frequency range of interest could reduce the related noise, it would simultaneously reduce the value of the real signal we want to probe. This means that the ultimate signal-to-noise ratio hence sensitivity would not be improved by a feedback acting on all frequencies.

As discussed in section 1.3 and observed in the above power spectra, the noise reduction when lowering the pressure inside the chamber is far smaller than expected:  $\sim$  one order of magnitude above. Although one could acquire data for longer month-long timescales as permitted by the stability of the trap in this experiment [32], understanding and reducing sources of noise appears to be the most interesting alternative to significantly improve the sensitivity of future acceleration measurements with reasonable integration times.

### 3.1.2 Laser pointing noise

It is known that laser beams present intrinsic pointing noise, i.e. angular fluctuations of the pointing of the laser. Among other reasons, these fluctuations generally originate from mechanical vibrations or thermal effects due to air currents [34].

As described in the schematic of the general optical setup in Figure 2.1, a four-quadrant photodetector (QPD) placed orthogonally to the axis of the trapping beam provides the power and the position of the pointing of the trapping beam. It is then possible to calculate the relative beam position stability of the trapping laser, defined as  $\Delta\alpha = 2\sigma_x/\omega_0$ , where  $\sigma_x$  is the standard deviation of the beam position and  $\omega_0$  the

waist of the beam at the trapping location [34]. A value of  $\Delta\alpha = 2 \times 10^{-6} / \sqrt{\text{Hz}}$  has been obtained in an experimental setup similar to this one [32], consistent with the noise at the spheres measured at low pressures.

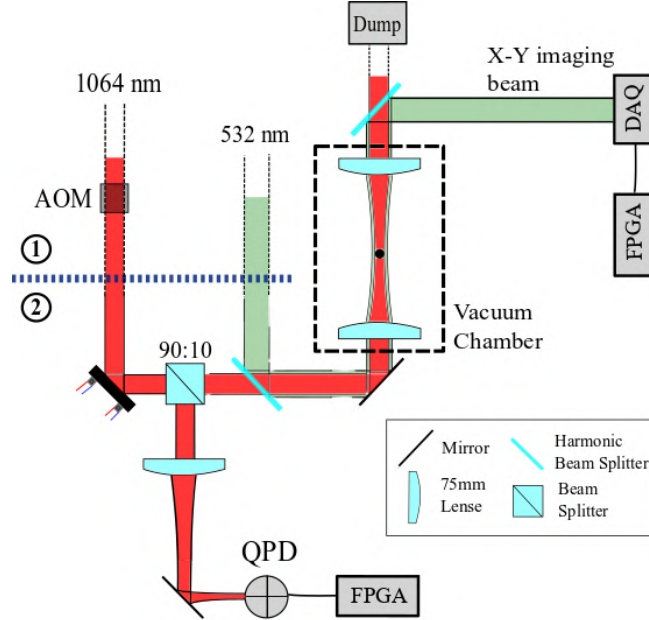


FIGURE 3.2: Zoom of the optical setup with a focus on the feedback system before the chamber. The QPD is positioned at the same focal distance as the trapping location inside the vacuum chamber so that it should in principle provide the pointing position of the trapping beam *at the trapping position*

One way to reduce the pointing noise of the trapping beam consists in applying an active feedback on the beam pointing position acquired by the QPD. Such a feedback was expected to stabilize the pointing position of the trapping laser and consequently the position of the sphere acquired at the output of the chamber. However, previous measurements indicated that this additional feedback did not improve the noise acting on the sphere. This observation led to the measurement of the correlation between the signal measured at the QPD in the X direction,  $X_{QPD}(t)$ , and the motion of the sphere measured by the data acquisition system (DAQ) after the chamber  $X_{DAQ}(t)$ .

The correlation between two signals  $x(t)$  and  $y(t)$  can be estimated by calculating the value of the coherence function  $C_{xy}(f)$  or normalized cross power-spectral correlation between both signals:

$$C_{xy}(f) = \frac{|S_{xy}(f)|^2}{S_{xx}(f)S_{yy}(f)} \quad (3.3)$$

where  $S_{xy}(f)$  is the cross power spectral density between  $x(t)$  and  $y(t)$  and  $S_{xx}(f)$  and  $S_{yy}(f)$  the power spectral densities of  $x(t)$  and  $y(t)$ , respectively. By construction,  $0 < C_{xy}(f) < 1$  and it indicates the correlation between  $x(t)$  and  $y(t)$ , maximized when  $C_{xy}(f) = 1$ . A coherence value  $< 1$  is on the other hand a strong indicator of the presence of different noises affecting the two signals.<sup>1</sup>

<sup>1</sup>A non-linear relation between  $X_{QPD}(t)$  and  $X_{DAQ}(t)$  would also imply a small coherence value, but no non-linear behaviour was detected in both signals.

In order to measure the coherence between  $X_{QPD}(t)$  from the four-quadrant photodiode and  $X_{DAQ}(t)$  from the X-direction sensor, a sphere was trapped at  $\sim 10^{-7}$  mbar and a 10Hz-sine wave with small amplitude was applied to the deflection mirror in the X direction and both signals recorded while  $\Gamma^{cool}(10\text{Hz}) \sim 0$  (Figure 3.3, left). Figure 3.3 (right) displays the coherence values in a range of frequencies. One notices that  $C_{X_{QPD}X_{DAQ}}(10 - 50\text{Hz}) \lesssim 10\%$  while  $C_{X_{QPD}X_{DAQ}}(10\text{Hz}) \sim 40\%$ , indicating that partially uncorrelated noises are affecting the two signals. More precisely and as drawn in Figure 3.3 (right), because  $X_{QPD}(t)$  and  $X_{DAQ}(t)$  follow different paths, any source of noise affecting one path but not the other would result in a coherence value  $< 1$ .

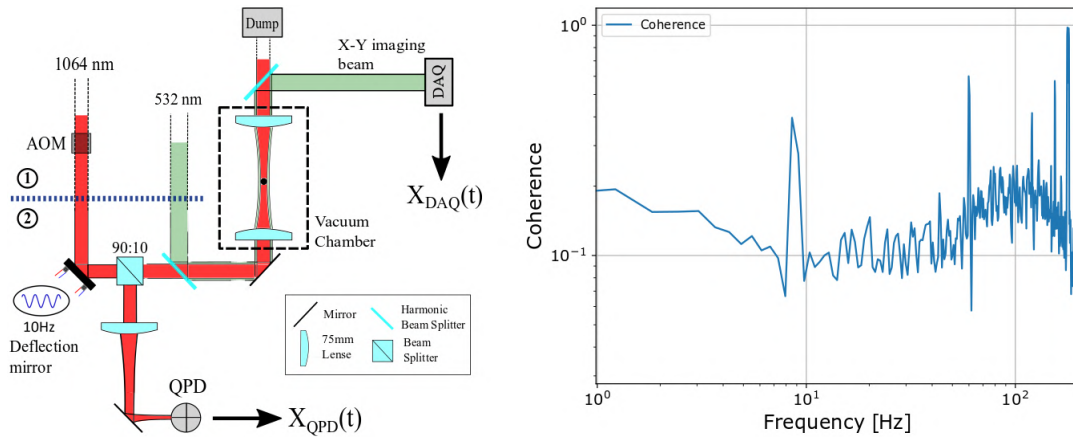


FIGURE 3.3: (left) Schematic of the test: a sphere is trapped at  $\sim 10^{-7}$  mbar and a small amplitude 10Hz-sine wave applied to the deflection mirror in the X direction. Both signals  $X_{QPD}(t)$  from the four-quadrant photodiode and  $X_{DAQ}(t)$  from the X-imaging sensor are acquired when the feedback system before the chamber is turned off. (right) Coherence function between  $X_{QPD}(t)$  and  $X_{DAQ}(t)$ . The coherence value at the excitation frequency  $C_{X_{QPD}X_{DAQ}}(10\text{Hz}) \sim 40\%$  while it does not exceed 10% in the range [10-50Hz].

One source of noise that could affect the imaging signal  $X_{DAQ}(t)$  but not  $X_{QPD}(t)$  is a noisy output imaging system, independent from the motion of the sphere. This contribution is relatively negligible however for as shown and explained in Figure 3.1, the spectrum of the imaging beam alone without sphere in the trap shows that all sources of noise in that case – vibrations of the optics, electronic noise for the overall detection system – are more than one order of magnitude below the actual measured noise for the sphere.

Another hypothesis suggested to account for noise that would affect  $X_{QPD}(t)$  and  $X_{DAQ}(t)$  independently in the range [10-50Hz], thus explaining why a coherence value  $< 1$  was measured, came from an additional observation. Adding to the features described above, a coupling was observed between the two co-aligned 1064 nm trapping and 532 nm vertical imaging beams even when there was no sphere in the trap. This observation was made through the following test. With no sphere in the trap and at high vacuum, a 10Hz sine-wave in the X-direction was applied to the deflection mirror and amplitude spectra for different configurations detailed in Figure 3.5 were plotted (Figure 3.4). As there was no sphere in the trap, the 10Hz excitation at the deflection mirror should normally have only affected the pointing position of the trapping laser and solely been recorded by the QPD. The

amplitude spectrum of the trapping beam recorded by the QPD before the chamber is drawn in yellow in Figure 3.4. The normal working configuration is drawn in Figure 3.5 (left), corresponding to the blue curve in Figure 3.4. When elongating the common path shared by the co-aligned trapping and imaging beams at the output of the chamber by displacing the harmonic beam splitter further away (centre, green curve), the response at 10Hz from the imaging beam became clearly visible. This indicates that the imaging beam is affected by the excitation from the deflection mirror, visible in  $X_{DAQ}(t)$  when the common path shared by both beam is long enough. To ensure that the 1064 nm trapping beam does not reach the X-sensor, the imaging beam was blocked before the chamber and the red bottom curve in Figure 3.4 was plotted.

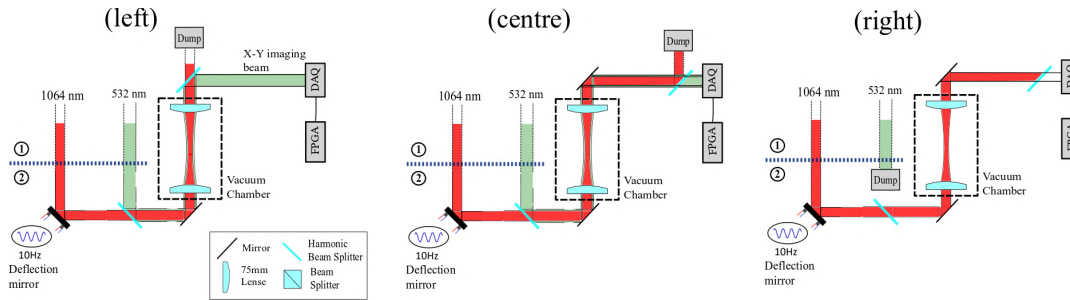


FIGURE 3.4: Different configurations to test the coupling between the co-aligned trapping and X-Y imaging beams. (left) Normal working configuration of the experiment. (centre) The beam splitter dividing the trapping and imaging beam is displaced further away from the output of the chamber, increasing the common path shared by both beams. (right) The imaging beam is blocked before the chamber to test if the 1064 nm trapping beam reaches the sensor.

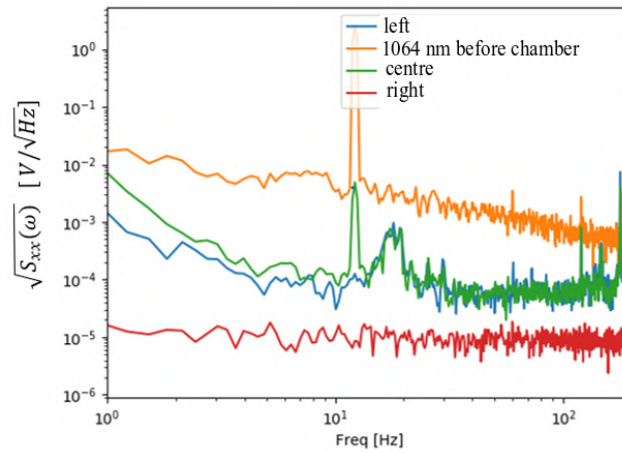


FIGURE 3.5: Amplitude spectra for different configurations when with no sphere in the trap and in high vacuum, a 10Hz sine-wave in the X-direction is applied to the deflection mirror. The different configurations are drawn in Figure 3.4. The yellow curve is the amplitude spectrum of  $X_{QPD}(t)$  while all other amplitude spectra are plotted from  $X_{DAQ}(t)$ .

To account for the existence of a coupling between the trapping and imaging beams, it was suggested that the trapping beam could communicate the excitation

from the deflection mirror to the imaging beam by producing air currents around it which would in turn communicate this excitation to the imaging beam. If true, any noise affecting the trapping beam on its way through the vacuum chamber could also affect the imaging beam and eventually  $X_{DAQ}(t)$ . Besides, if the 1064 nm trapping beam induces noise at the 532 nm imaging beam, it could also induce noise at itself: noise at the trapping beam could be communicated to air molecules around it which would in turn cause additional noise at it. If true, this hypothesis could explain why different noises are induced at signals  $X_{QPD}(t)$  and  $X_{DAQ}(t)$ , hence the small coherence value between them.

If the hypothesis of an air-induced noise is true, reducing the pressure on the path of the co-aligned beams should lead to a reduction of the overall noise reaching the imaging sensors. A further test was thus performed: a 10Hz oscillatory displacement of the 1064nm trapping beam through the deflection mirror was applied as before and the pressure inside the chamber was progressively lowered from atmospheric pressure down to  $10^{-5}$  mbar. Figure 3.6 shows the voltage amplitude of the signals reaching the sensors at the output of the vacuum chamber at 10Hz for each direction, plotted for different pressure values and with the associated noises. Particularly visible for  $X_{DAQ}(t)$  and  $Y_{DAQ}(t)$  corresponding to the vertical imaging beam co-aligned with the trapping beam and thus sharing the longest optical path with it, the response at 10Hz decreases by one order of magnitude across the decreasing of the pressure from  $10^3$  to 1mbar. This result is consistent with the assumption according to which air molecules are the mediators which transfer the laser pointing noise to the imaging beam. In the case of  $Z_{DAQ}(t)$  for which only a short optical path is shared with the trapping beam, the response at 10Hz is constant through the range of pressure values. For this measurement,  $\sim 10\%$  of the X-Y imaging beam is still co-aligned with the trapping beam outside the chamber. If the hypothesis of an air-induced noise holds, the results in this plot cannot be fully attenuated.

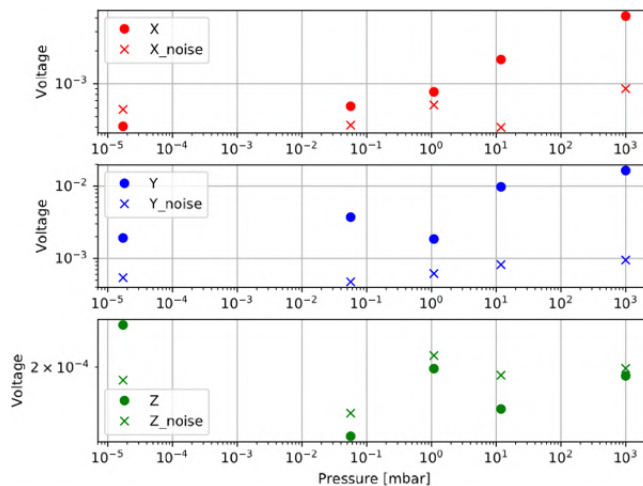


FIGURE 3.6: Voltage amplitude of the signals reaching the sensors at the output of the vacuum chamber at 10Hz, when progressively decreasing the pressure inside the vacuum chamber from atmospheric pressure to  $10^{-5}$  mbar.

The above discussions motivate the hypothesis of an air-induced laser pointing noise communicated from the trapping beam both to itself and the imaging beam. The random nature of noise would explain why partially uncorrelated noise affects the signals acquired by the QPD and the DAQ, leading to an ineffective feedback

loop at the QPD. The current experimental setup already uses a harmonic beam splitter right at the output of the chamber to reduce the common path shared between the co-aligned trapping and imaging beams. It is therefore believed that in order for the feedback system before the chamber to be implemented efficiently, one must isolate the trapping beam from a high pressure environment by enclosing the input optics of region 2 in Figure 2.1 in a vacuum chamber.

## 3.2 Pre-chamber: design and manufacturing

In order to test the hypothesis of an air-induced laser pointing noise, we design and implement an isolation system for the trapping laser beam before the vacuum chamber. As this isolation system takes the form of a vacuum chamber for the input optics, it will be referred as the *pre-chamber* in the following sections, whereas we will refer to the existing vacuum chamber as the *main chamber*.

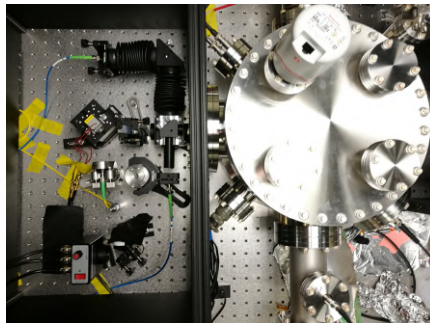


FIGURE 3.7: Top view of the input optics presently enclosed in a black box (left, corresponding to region 2 drawn in Figure 2.1) and the main chamber (right, cylindrical shape).

The first part of this thesis was devoted to the design of the pre-chamber and ordering of all the materials needed to achieve its construction. When writing this report, the pre-chamber has just been manufactured and last tests are being performed in order to ensure it presents no leaks, before installing it on the optical table.

### 3.2.1 Design of the pre-chamber

Figure 3.8 shows photographs of the input optical setup corresponding to region 2 drawn in Figure 2.1. On the right, a zoom focused on the input of the main chamber. As no major modifications of the physical configuration of the input optics are expected, the existing configuration has been set as a reference to shape and size the pre-chamber (Figure 3.8, left).

Although lower is the pressure inside the pre-chamber, lower is the expected pointing noise, a pressure lowered down to  $10^{-2}$  mbar is assumed to be enough to significantly reduce the air-induced pointing noise of the trapping laser beam (see Figure 3.6). This means that the pre-chamber is not expected to sustain high vacuum, contrary to the main chamber which works at pressures as low as  $< 10^{-7}$  mbar. Besides, as designing a high-vacuum chamber is far more delicate and expensive, especially because all elements inside must be vacuum-compatible, a mere extension of the main chamber is not desirable. This would furthermore add a significant volume to be pumped down to  $10^{-7}$  mbar and thus considerably slow down each execution of a trapping process.

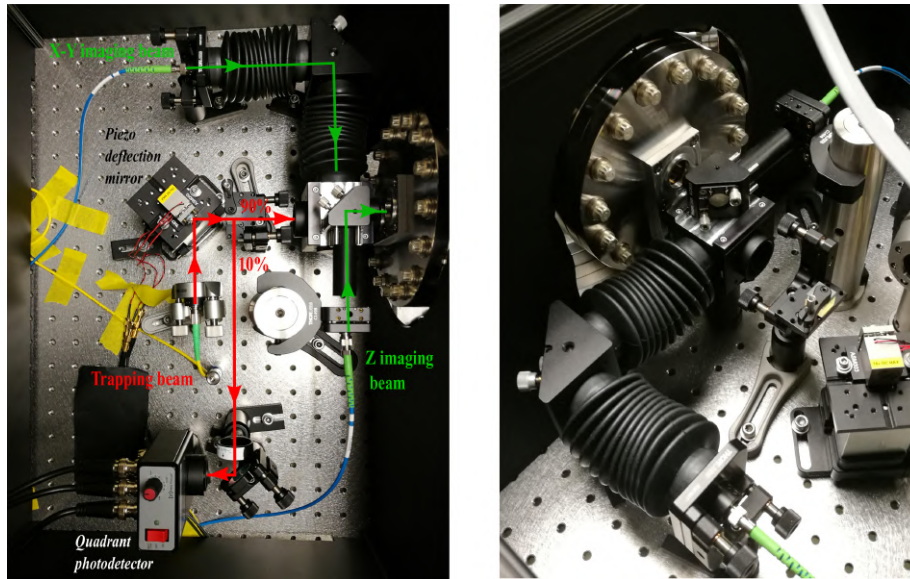


FIGURE 3.8: (left) Photograph of the input optics, corresponding to region 2 in Figure 2.1 of the general optical setup. (right) Zoom of the left photograph, focused on the contact area between the future pre-chamber and the main-chamber.

### 3.2.2 Connection to the main chamber and sealing

As shown in Figure 3.8, the incoming 1064nm trapping and 532nm imaging beams reach the main chamber through two windows located on the disk surface of a 6" CF flange, fixed to the main chamber. Through the lower window pass the co-aligned 1064nm trapping and 532nm X-Y imaging beams, while the 532nm Z imaging beam passes through the upper one. These two windows cannot be obstructed, meaning that the connection between the pre-chamber and the main chamber must be ensured by proper sealing.

Figure 3.9 shows a Solidworks drawing of the adopted sealing option. On the outer face of the pre-chamber intended to be in contact with the main chamber, a circular hole with diameter 3.75" is co-centred with the 6" flange of the main chamber to encircle the two windows. To ensure sealing, a groove concentric to the hole is milled to host a circular Viton® sealing O-ring. The optimal depth of the groove knowing the thickness of the sealing O-ring is tabulated and can be found in [37]. An additional outer groove is milled to fit the circularly-patterned screws that hold the 6" input flange to the main chamber (see Figure 3.8, right).

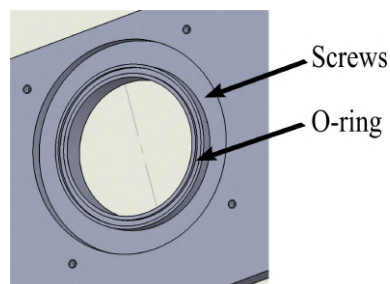


FIGURE 3.9: Drawing of the face of the pre-chamber in contact with the main chamber

As already discussed, the shape and size of the pre-chamber are constrained by the spatial configuration of the existing input optical setup. A rectangular-shaped pre-chamber with external dimensions 22"x15.5"x8.5" easily satisfies this constraint. Although a cylindrical shape is more robust to hold wall stresses due to vacuum, a circular bottom surface would imply a considerable ratio of dead surface regarding the positioning of the optics. Such dead space would require a bigger therefore more expensive as well as heavier pre-chamber.

Figure 3.10 shows a three-dimensional view of the pre-chamber and a top view of the assembly between the pre-chamber and the main chamber, respectively.

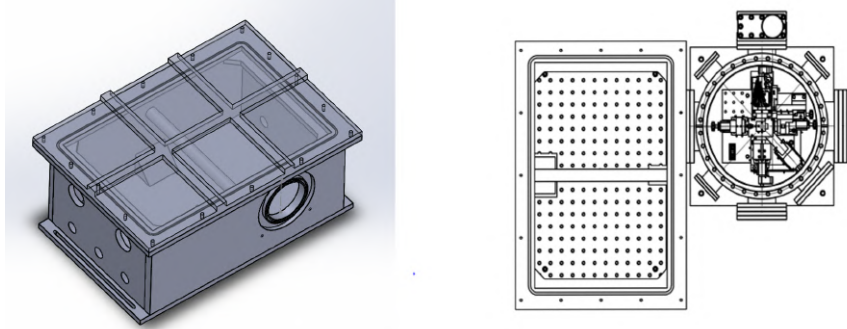


FIGURE 3.10: (left) 3D Solidworks view of the pre-chamber. (right) Top view drawing of the prechamber when assembled with the main chamber.

Standard vacuum chambers with this size and wall thickness 0.5" are generally robust enough to avoid implosion. However, as the pre-chamber is intended to contain an optical setup, minimum bending of the bottom plate is required in order to minimize misalignment of the optics. A 1" bottom surface and 0.75" thick wall for the surface to be sealed with the main chamber were adopted. All other walls are 0.5" thick. Finite element calculations have been performed on Solidworks to evaluate stresses and wall displacements for three different materials commonly used for vacuum chambers. Table 3.1 displays different characteristics and results for these materials. A pressure load of 1atm was used while the total mass was calculated considering a unique material.

	Acrylic	6063-T6 Aluminum	Steel304 (SS)
Mass Density ( $kg/m^3$ )	1200	2700	8000
Elastic Modulus ( $10^9 N/m^2$ )	3	69	190
Yield strength ( $10^6 N/m^2$ )	45 (13.4)	215 (13.4)	207 (13.4)
Max displacement at the bottom	$< 800\mu m$	$< 40\mu m$	$< 10\mu m$
Max displacement on the contact surface	$< 200\mu m$	$< 2\mu m$	$< 2\mu m$
Pre-chamber total mass (kg)	16	37	104

TABLE 3.1: Properties of three materials commonly used to build vacuum chambers. Data were taken from the Solidworks library. Calculations of the stresses and displacements at both the bottom surface and sealing area, as well as the total mass of the pre-chamber, were performed on Solidworks. The yield strength of the different materials are to be compared to the maximum stress applied to the walls of the chamber and calculated to be  $13.4 \times 10^6 N/m^2$ .

SS304, showing minimum displacements at both the bottom plate and sealing area, was eventually adopted. Figure 3.11 shows the results from calculations of stresses (left) and displacements (right) using SS304. Results from these calculations also show that additional supporting parts are necessary to minimize bending of both the bottom plate and the sealing area. A 0.5" thick aluminium lid can be screwed to the top of the pre-chamber, while sealing is ensured by an O-ring placed in a groove milled all around the perimeter of the top surface (see Figure 3.10, right). This choice implies a total weight of  $\sim 91\text{kg}$  when opting for an aluminum lid. An unanodized aluminum breadboard will be screwed to the bottom surface of the pre-chamber to allow precision alignment of the optics (see Figure 3.10, right). Eventually, five holes are drilled on the left and right faces of the pre-chamber to host KF-flanges for wire and fiber connections as well as connections to the pump.

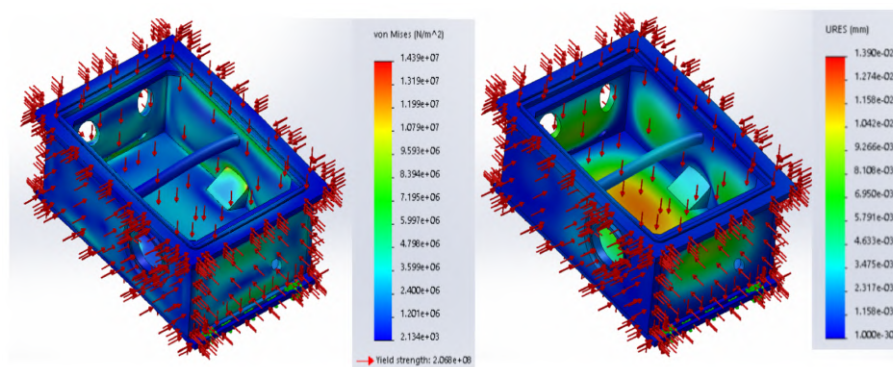


FIGURE 3.11: Results from calculations of the stresses and displacements for the final pre-chamber. The aluminum lid was included in the calculation and hidden for the final display.

### 3.2.3 Pre-chamber manufacturing

Materials suppliers include: Kurt J. Lesker, McMaster-Carr and Accu-Glass Products Inc. for vacuum-compatible components, Thorlabs Inc. for optics-related components, Digi-Key for electronics. Yale University hosts the J.W. Gibbs Professional Shop, a machine shop run by external, professional machinists who can provide precision machining for experiments led within the university. Figure 3.12 shows the cutting of stainless-steel plates into walls of the chamber intended to be further machined and welded. This cutting procedure was performed using water-jet cut technology (at Wright Laboratory). Figure 3.13 shows a picture of the manufactured pre-chamber.



FIGURE 3.12: Photographs of water-jet cut SS304 plates. The right picture was taken after flushing from the surface of the plates the water/abrasive mixture sprayed out from the jet cutter.



FIGURE 3.13: Photograph of the manufactured pre-chamber. Tests are currently being performed in order to ensure it presents no leaks before moving it onto the optical table.



## Chapter 4

# Mass attractor for short-range gravity measurements

The second part of this thesis was devoted to the assembly of a beforehand designed mass attractor prototype, on which preliminary tests were then performed.

### 4.1 Introduction

Figure 4.1 gathers the current submillimetric exclusion plots as a function of  $|\alpha|$  and  $\lambda$  where experiments have already refuted Yukawa-like potentials as corrections of the Newtonian gravitational potential. Therefore, exploring new parameter spaces at micron-sized scales always requires higher sensitivity than previously reached [13], [15], [16], [38]. Due to the weakness of gravitational interactions at these length scales, new experiments involving optical levitation of microspheres reveal delicate technical challenges of both building appropriate test masses and overcoming all sources of noise and background.

In the previous section, the design of a pre-chamber was motivated by the possibility of reducing a first-order noise believed to originate from the pointing noise of the trapping laser and eventually increasing sensitivity. In this section, we describe the motivations and building of a test mass to measure gravitational interactions in new parameter spaces at micrometer scales.

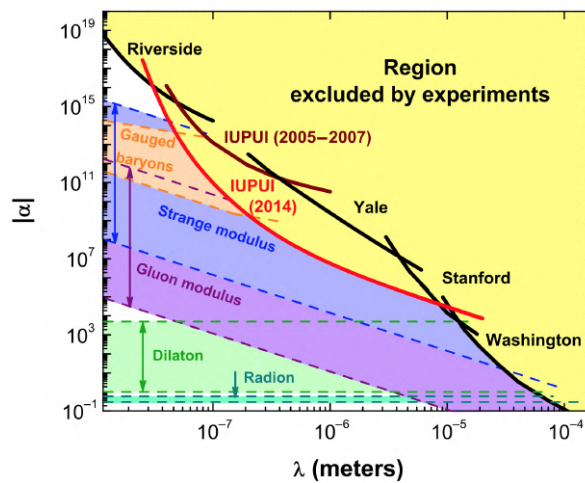


FIGURE 4.1: Parameter space as a function of  $|\alpha|$  and  $\lambda$  experimentally excluded in the search for Yukawa-type non-Newtonian gravitational potentials  $V = -\frac{Gm_1m_2}{r}(1 + \alpha e^{-\frac{r}{\lambda}})$ , focused on the sub-millimetre length scales [13].

## 4.2 Discussion on the design of the mass attractor

In order to test gravity in new parameter spaces at micron-sized scales using optically levitated microspheres as acceleration sensors, a known gravitational field must be applied to the sphere while measuring its motion response. Because a Yukawa-like deviation of the Newtonian gravitational potential decreases exponentially for a given characteristic distance  $\lambda$ , this mass attractor must be brought as close as possible to the sphere. This can be achieved by bringing to the vicinity of the sphere a mass attractor generating an alternative gravitational field.

Due to this proximity, the design of a mass attractor must anticipate and minimize all sources of noise and background that could appear when approaching it to a trapped sphere. As discussed in section 2.3, even a discharged sphere couples to the surrounding electromagnetic field through its permanent and induced dipoles. For this reason, the mass attractor is generally made of a grounded conducting body [8]. Besides, the presence of Casimir forces due to fluctuations of the electromagnetic field and the presence of patch potentials, i.e. microscopic inhomogeneous electric potentials at the surface of any material, have been measured at these length scales [38], [39]. As gold presents comparatively small patch potentials, the mass attractor is generally gold-plated [8]. Casimir forces can be screened by placing a shield between the test mass and the sphere, but this option also sets a limit on the minimum approaching distance between them.

Eventually, because of the presence of the above cited electric fields, experiments using a moving mass attractor face the problem of electrical coupling with the sphere at the oscillating frequency, which means a background at the frequency of interest that would therefore compete with the real signal [40]. Such an oscillating attractor would also scatter the light surrounding the sphere at its frequency, thus creating an optical coupling adding to the electrical one. For these reasons, this experiment opted for a still mass attractor.

## 4.3 Principle of the experiment

The mass attractor designed in this experiment being still, the oscillating gravitational field is generated by a flow of droplets made of two immiscible liquids of different densities inside a still capillary (Figure 4.2). This alternating flow should ideally be adjustable in a range of frequencies spanning a few up to 70 Hz, i.e. within the frequency range in which the centre of mass of a trapped microsphere could respond without being damped by the feedback system.

In order to minimize the distance between the sphere and the flowing droplets, capillaries with thinnest possible walls are desired. Three polycarbonate capillaries (Paradigmoptics) with different internal and outer diameters (ID and OD respectively) are to be tested:  $50\mu\text{m}$  ID/  $56\mu\text{m}$  OD,  $50\mu\text{m}$  ID/ $60\mu\text{m}$  OD and  $90\mu\text{m}$  ID/ $100\mu\text{m}$  OD. The last and biggest one presenting lower impedance hence easier to test, was used for the first tests.

Different plots in Figure 4.3 show the projected limits for this experiment, calculated using current acceleration sensitivities for  $15\mu\text{m}$  size spheres. The detailed derivation is gathered in Appendix C. A density difference  $\Delta\rho = \rho_1 - \rho_2 = 1.2\text{g/mL}$  was used.

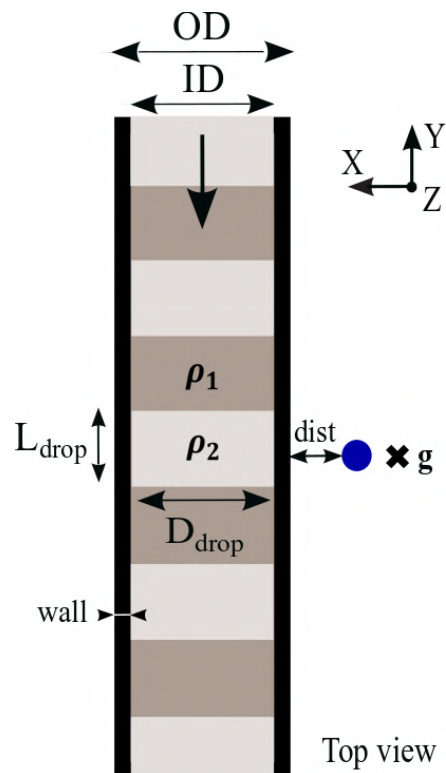


FIGURE 4.2: Schematic of the working principle for the adopted mass attractor from a top view. A capillary with outer diameter OD and internal diameter ID is positioned  $dist$  away from the sphere, where  $dist$  is the minimum distance between the external wall of the capillary and the surface of the sphere. Through this capillary, a flow of immiscible droplets is generated at tuneable frequencies in the frequency range below  $\sim 70\text{Hz}$  to create an alternating gravitational field in the vicinity of the sphere.

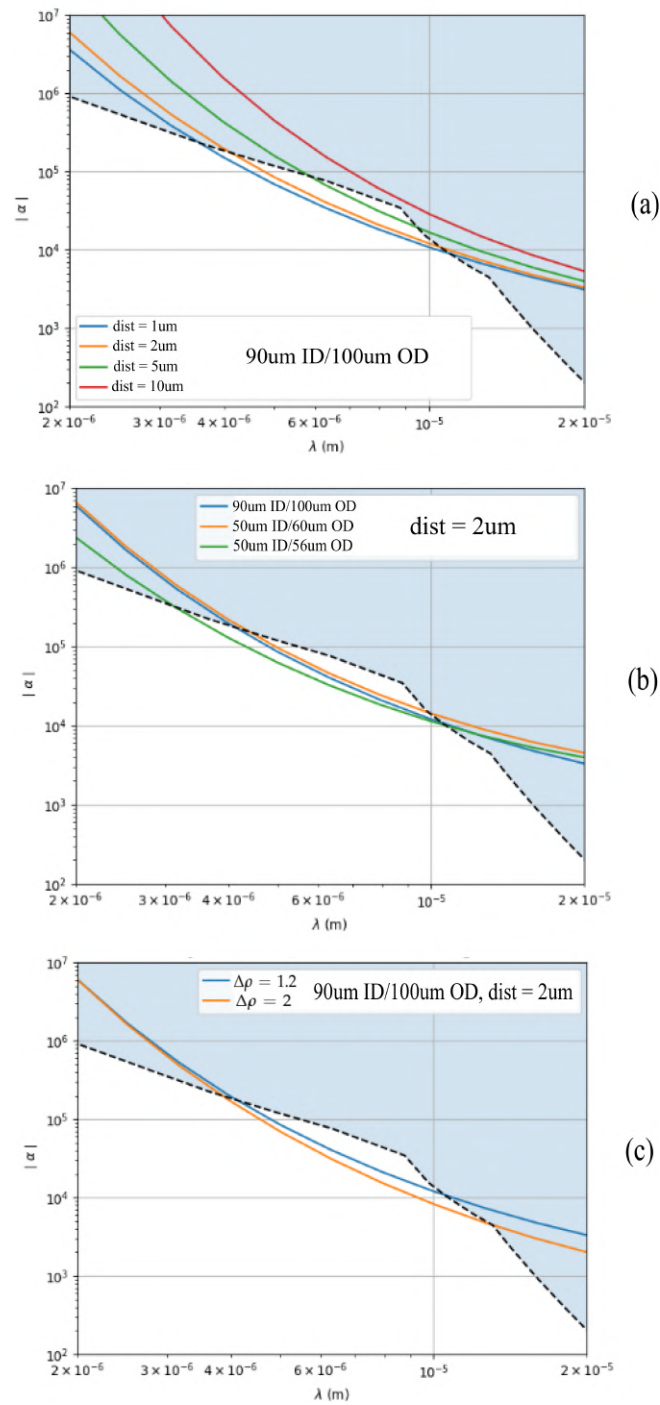


FIGURE 4.3: (a) Predicted limits for the  $90\mu\text{m}$  ID/ $100\mu\text{m}$  OD capillary approached at different distances to a trapped sphere with diameter  $15\mu\text{m}$ . The shaded blue area corresponds to the already excluded parameter space [13]. As expected from the exponential behaviour, closer the droplets are to the sphere, larger parameter space can be explored and no improvement is made for this capillary when  $\text{dist} > 10\mu\text{m}$ . (b) Predicted limits for the three available capillaries when approached  $2\mu\text{m}$  away from the sphere. A thinner wall and a bigger droplet diameter seem more interesting. (c) examines the case of two different density differences  $\Delta\rho = 1.2$  and  $\Delta\rho = 2$ : as expected, the greatest density difference is sought.

## 4.4 Experimental Methods

### 4.4.1 Droplets generator

The designed mass attractor consists of a continuous flow of immiscible phase droplets with different densities, thus providing an oscillating gravitational field near a trapped microsphere. Two immiscible solutions of mineral oil ( $\rho_{oil} = 0.8g/mL$ ) and deionized water ( $\rho_{water} = 1.0g/mL$ ) were introduced into a microfluidic droplet generator (Elveflow) to generate highly monodisperse droplets (see Figure 4.4). In order to obtain more stable droplets, a surfactant composed of Span and Tween to ratio 3 : 4 in volume was added to the deionized water solution to a volume ratio of 1:100.

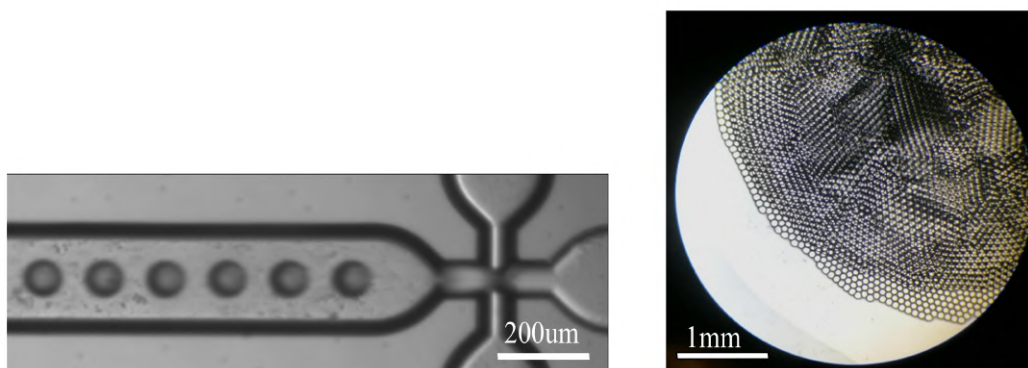


FIGURE 4.4: (left) Microscope image of oil droplets generated using a microfluidic chip. (right) Microscope image of a drop of the obtained emulsion. The droplets thus generated appear monodisperse and the emulsion remains stable for several weeks when stored in a closed test tube.

Mineral oil and aqueous solutions are pumped from their initial recipients using a pressure controllable system provided with the microfluidic chip (Figure 4.4). The flow is generated by monitoring the input pressure.

Using this apparatus, droplets of consistent sizes with tuneable radiuses from  $\sim 30\mu m$  up to  $\sim 80\mu m$  are easily generated. The finally obtained oil/water emulsions remained stable several weeks when stored in closed test tubes.

### 4.4.2 Heavy Liquid

The denser phase of the mass attractor is obtained by mixing the oil/water emulsion obtained from the droplets generator with an almost saturated aqueous solution of lithium heteropolytungstate crystals, or *LST Heavy Liquid*. A maximum density of 2.85g/mL can be reached if used undiluted.

As a highly saturated solution, a drop of heavy liquid under a microscope shows the development of salt crystals within few minutes after exposure to ambient air. Figure 4.5 shows a drop of pure (left) and diluted (right) heavy liquid deposited upon a drop of oil/water emulsion few minutes after deposition. The aqueous phase spreading around the emulsion develops into LST crystals, whereas within the emulsion oil droplets are progressively “caught” by the developing crystals of the aqueous phase. Such a hardened, solidified emulsion being unoperable<sup>1</sup>, the

<sup>1</sup>The salt may flow if the pressure is high enough, but undesirable consequences may also occur, such as clogging inside the capillary.

heavy liquid must be diluted in deionized water using a systematic approach to determine the maximum attainable density difference between oil and aqueous phases while maintaining an operable emulsion which could smoothly flow within a  $90\mu\text{m}$  ID capillary.

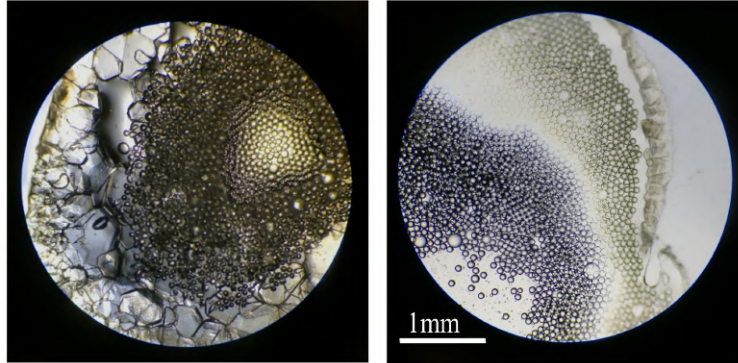


FIGURE 4.5: Pictures of a drop of pure (left) and diluted (right) heavy liquid deposited upon a drop of oil/water emulsion few minutes after deposition. The aqueous phase spreading around the emulsion develops into LST crystals, whereas within the emulsion oil droplets are progressively “caught” by the developing crystals of the aqueous phase.

The addition of heavy liquid also seemed to make the oil droplets more fragile, becoming more easily breakable when stirring a sample of the emulsion, contrary to the initial oil/water emulsion. This factor was also considered for the systematic determination of the maximum reachable density.

The finally reached maximum density for the aqueous phase approximates  $\sim 1.9$  g/mL, assuming that the heavy liquid homogeneously mixes within the aqueous phase of the emulsion. This corresponds to a density difference with the oil droplets  $\Delta\rho = 1.1\text{g/mL}$ . This was realized by diluting the heavy liquid within deionized water with a volume ratio 50 : 50. This diluted solution is then mixed in large volume ratio ( $V_{\text{water}} : V_{\text{heavyliquid}} > 10 : 1$ ) to the emulsion. To obtain the precise densities of both phases, necessary for the final experiment, it is possible to strongly stir the final solution to destroy the droplets until two immiscible phases form again. Measuring the respective densities of both phases should give a reasonable approximation of the densities of the droplets.

#### 4.4.3 Detection system

In order to get access to the gravitational field generated by the flowing droplets, a detection system is designed to locate the positions of the droplets once the capillary is positioned inside the main vacuum chamber. Figure 4.6 shows the principle of this detection system, relying on the difference in refractive index between the two immiscible phases composing the droplets. By approaching the tip of an optical fiber close to the flow and collecting the back reflected light, one should be able to distinguish one phase from another. In the final experiment, the response motion of the sphere to the generated gravitational field is measured by calculating the correlation between the signal from the optical fiber detecting the droplets  $X_{\text{drop}}(t)$  and  $X_{\text{DAQ}}(t)$ . Therefore, even a non uniform flow of droplets, leading to non-periodic signals, can be detected and post-processed using this detection system.

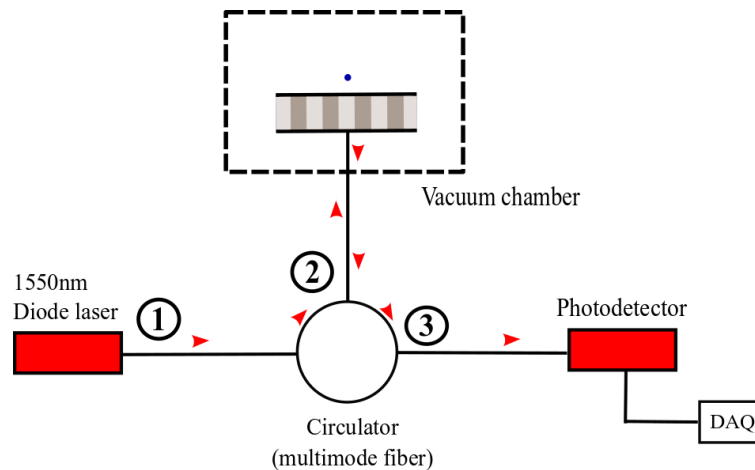


FIGURE 4.6: Schematic of the detection system adopted to detect the position of the flowing droplets once the capillary is positioned inside the main chamber. A 1550nm laser diode is coupled to an optical fiber connected to the first port of a fiber circulator. A fiber circulator consists, in our case, of three ports from which light is transmitted successively in a one-way direction. The detecting fiber positioned close to the flowing droplets is connected to the second port of the circulator, so that if the light transmitted from port 1 to the detecting fiber through port 2 is reflected back when reaching the capillary's surface, the reflected light is necessarily carried to port 3. A photodetector collects the reflected light and the converted electrical current sent to the DAQ.

#### 4.4.4 Capillary Holder

Because the capillary is expected to approach the trapped sphere as close as possible, a capillary holder was designed using Solidworks and fabricated within the Gibbs professional shop hosted by Yale University. As discussed in section 4.2, the mass attractor should ideally be a grounded gold-plated conductive body to minimize electrical backgrounds. The capillary holder has therefore been manufactured using aluminum, with room left to be grounded (see Figure 4.8). Although the capillary is made of polycarbonate, it will be gold-coated before being introduced inside the main chamber.

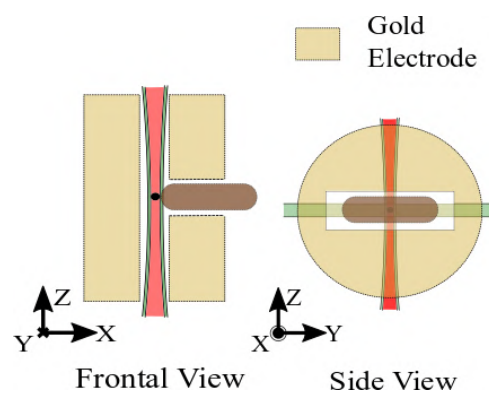


FIGURE 4.7: Frontal (left) and side (right) views of the vicinity of the sphere when a holder approaches close enough to the sphere. The tip is seen to obstruct the paths of both X-Y and Z-imaging beams, creating sources of complex background signals due to light scattering.

As shown in Figure 4.7, if the holder tip is brought close enough to the sphere, it would block and scatter the light of both the X-Y and Z imaging beams, thus generating background signals. This is the reason why a specific shape was designed for the holder tip, semi-circular in the X-Y plane and as thin as the thickness of the capillary in the Z-axis. The detailed design of the capillary holder is shown in the 3D Solidworks image of Figure 4.8 (left).

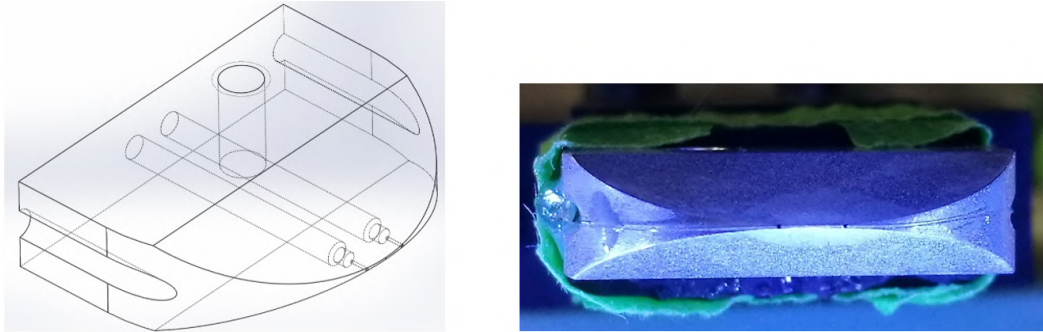


FIGURE 4.8: (left) Solidworks 3D view of the capillary holder, a 0.75" large, 0.2" thick piece which presents a semi-circular shape tip pierced with two 0,004" diameter holes separated one from another by a distance of 0.1". A capillary with 90 $\mu$ m (0.035") ID and 100 $\mu$ m (0.39") OD is positioned around the curved face, all the way to the two 1/16" diameter grooves at the edge of the holder that support a bigger, 0.01" ID, 1/16" OD tube to which the capillary is glued with epoxy. The two central holes are equally distant from the tip end and are intended to hold two imaging optical fibers. All the way in the backward direction, increasing diameters are incrementally designed to host ferules which hold and stabilize these fibers. A cylindrical hole is added on the upper surface of the holder to leave room for electrical grounding of the overall piece, made of aluminum. (right) Photograph of the front of a prototype of the capillary holder. The two central holes are visible, as well as the capillary touching the edge of the holder, glued with epoxy around the tip.

The manufacturing represented a great challenge due to high precision requirements, especially regarding the sharpness of the tip end and the required alignment for the cylindrical holes supporting the optical fibers. Figure 4.8 (right) is a picture of the front of the holder tip with a capillary positioned around it and glued to two supporting tubes placed along the milled grooves. The optical fibers are inserted from the backside of the holder where they are glued with epoxy.

#### 4.4.5 Preliminary tests

As described in section 4.4.3, the two optical fibers fixed into the capillary holder represent the detecting system measuring the position of the droplets to be solely relied on in the final experiment. In order to test their reliability in sensing the flowing droplets, preliminary tests were performed outside the main chamber by comparing the signal at the photodiode with a video recorded by a microscope camera. A detailed description of the test is given in Figure 4.9.

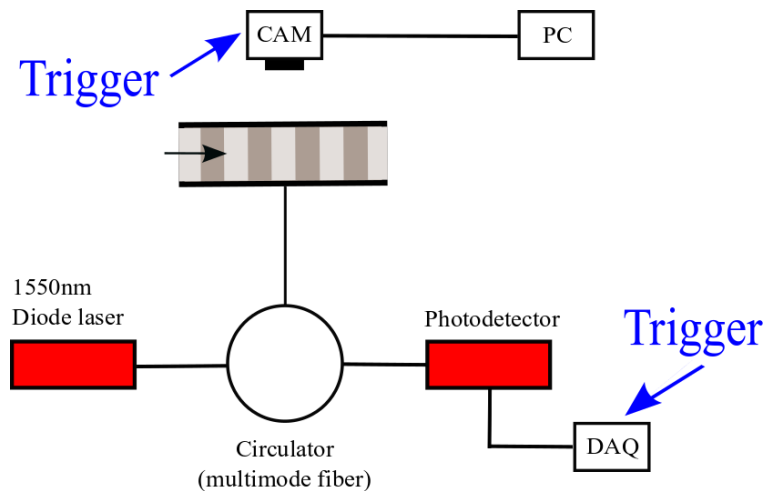


FIGURE 4.9: Schematic of the preliminary tests. A CCD camera is positioned above the tip of the capillary holder to image the droplets flowing through the capillary. Image frames from the camera (CAM) are recorded at 350Hz using a trigger mode synchronised with the rising edges of a 350Hz square wave delivered by an AC voltage supply. On the side of the DAQ, a trigger mode is also used to start acquisition with the first rising edge of the square wave when activating the output of the voltage supply. These synchronisations ensure simultaneous start times for the CAM and the DAQ. The sampling rate of the DAQ is tunable and is set to be higher than the camera's framing rate, at 1000Hz. Mismatch in the sampling rates of the CAM and the DAQ is corrected when analysing data with Python.

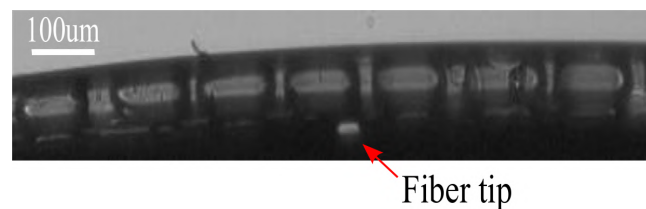


FIGURE 4.10: Image frame of a  $90\mu\text{mID}/100\mu\text{mOD}$  capillary with oil/water droplets flowing. The tip of the optical fiber is clearly visible.

Figure 4.10 shows an image frame from the camera, where the tip of a fiber is clearly visible. A code was implemented in Python to associate each image frame with an acquired datum from the photodiode and display the whole as a video. Frames of this video are shown in Figure 4.11 for droplets flowing at 10Hz. A current amplifier was designed to amplify the output current of the photodiode sent to the DAQ. A correlation appears between both frames when playing the whole video

to attest the reliability of the detection system in the case of an oil ( $n_{oil} = 1.47$ )/water ( $n_{water} = 1.33$ ) emulsion.

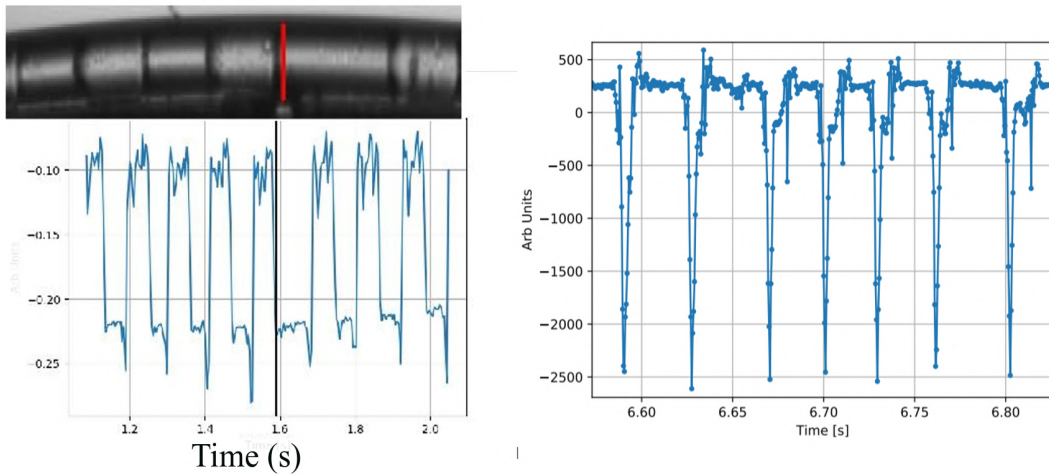


FIGURE 4.11: (left) Video frame displaying an image frame from the camera with the synchronized datum from the DAQ. The passing droplets were clearly visible from the output signal of the optical fiber, showing a flow at frequency  $\sim 10\text{Hz}$ . (right) Signal from the optical fiber when the flow rate is increased up to  $\sim 30\text{Hz}$ .

Distinguishable flow frequencies up to  $30\text{Hz}$  were reached using the oil/water emulsion (Figure 4.11, right). A larger range of frequencies within  $[0 - 40\text{Hz}]$  is sought, more specifically using the heavy liquid. These tests are being performed, in parallel with the addition of the second fiber to form a timing system.

#### 4.4.6 Flow generation system improvement

For these preliminary tests, an oil/water emulsion was flowed in the capillary using a pressure controller providing a maximum pressure difference of  $\Delta P = 2$  bars. This pumping system, acting as a voltage source in the equivalent electrical circuit model, did not allow operable flow currents when pumping the more viscous heavy liquid/oil emulsion. Considering the flow of the oil/heavy liquid emulsion laminar, the Hagen-Poiseuille equation seems a reasonable approximation to describe the flow inside the capillary. Within this approximation and for a given desired volumetric debit  $Q$ , the required pressure difference  $\Delta P$  between two ends of a tube is proportional to the tube's length  $L$  and the inverse fourth power of the radius  $R$  of its cross section:

$$\Delta P \propto \frac{LQ}{R^4} \quad (4.1)$$

With oil/water emulsions, volumetric flows around  $900\mu\text{L}/\text{hr}$ , calculated from the recorded videos, was reached at  $30\text{Hz}$ . To reach similar volumetric flows with the heavy liquid emulsion and ensure a more stable flow rate, the Elveflow pumping system was replaced by a syringe pump. This new scheme is expected to provide steady flow in a range  $[0.73 - 1.5 \cdot 10^6 \mu\text{L}/\text{hr}]$ . Tests are currently being performed.

#### 4.4.7 Preliminary background tests inside the vacuum chamber

A gold-plated replica of the holder alone (without capillary and flowing droplets) was positioned inside the chamber. With the use of a piezo stage, it was approached to a trapped sphere with diameter  $\sim 23\mu\text{m}$  at  $< 10^{-7}\text{mbar}$  to perform preliminary tests and identify possible sources of noise and background.

As discussed in section 4.4.4, even a thin and semi-circular shaped holder tip blocks and scatters part of the two imaging beams when the holder approaches the sphere close enough. Especially in the X direction along which the holder moves, this means that at short distances from the sphere, the X-BPD not only acquires the position of the sphere but also includes the presence of the holder. When sent to the X-FPGA, the feedback is not performed on the real position of the sphere. While creating noise and backgrounds, this also caused the sphere to be lost at a distance  $\sim 20\mu\text{m}$  from the holder during the first tests.

In order to reduce this effect, a pinhole was placed before the input of the X-BPD to reduce and focus the transmitted light to a tight area around the image of the sphere (see Figure 4.12). This allowed us to approach the holder as close as  $\lesssim 4\mu\text{m}$  to the sphere (see Figure 4.13). A precise determination of their relative distance is currently limited by the resolution of the optical imaging system.

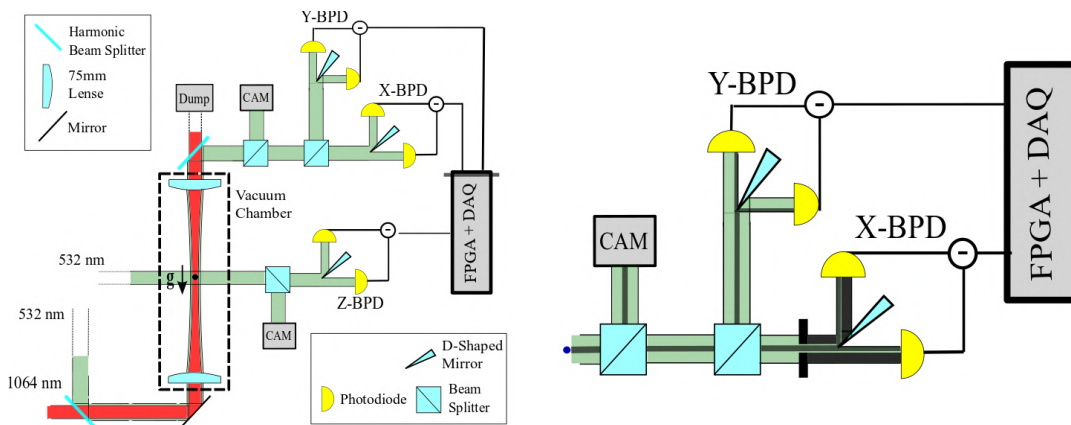


FIGURE 4.12: (left) schematic of the general optical setup. (right) Focus on the output optics of the X-Y imaging system. The shaded lines correspond to the imaged position of the sphere. In the X direction, a pinhole is placed before the D-shaped mirror to solely collect the light transmitted from a tight area around the image of the sphere.

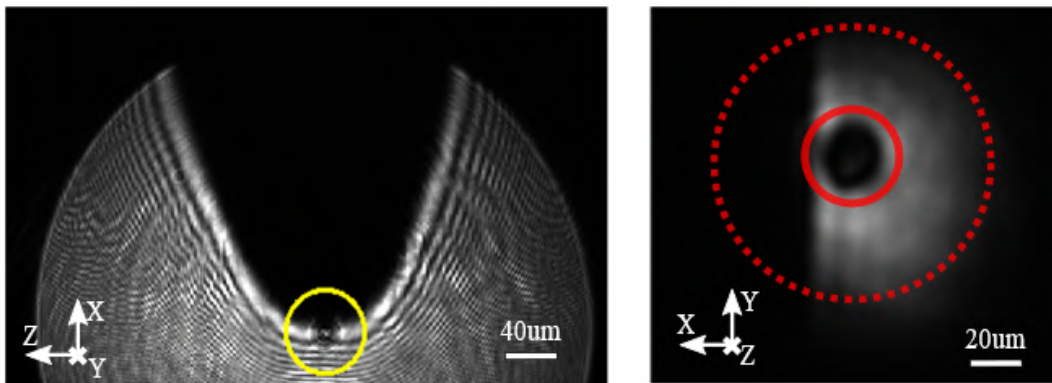


FIGURE 4.13: Images of the capillary holder close to a trapped sphere, recorded by the two CCD cameras at the output of the main vacuum chamber. (left) Image of the vertical X-Z plane transmitted from the Z-imaging beam. (right) Image of the horizontal X-Y plane transmitted from the X-Y imaging beam. When a smaller pinhole (red plain lines) is used, the light coming to the X-BPD is reduced and more focused on the sphere alone. When there is no pinhole or when using bigger ones (red dotted circle), the X-BPD hence the X-FPGA are affected by the approach of the holder, leading to a rapid loss of the sphere. The estimated minimum distance between the capillary holder and the sphere on these pictures is  $\sim 4\mu m$

## Appendix A

# PID Feedback system

As we saw in Equation 1.9, the additional damping generated to counteract the heating of the sphere's center-of-mass when the pressure inside the chamber is lowered takes the form:

$$F^{cool} = -\Gamma^{cool} \frac{dx}{dt} \quad (\text{A.1})$$

As it is proportional to the velocity of the sphere, it can be achieved using the derivative part of a proportional-integral-derivative (PID) controller delivered through the FPGA.

For each direction of space, a PID controller takes as an input the error signal  $e_x(t)$ :

$$e(t) = x_0 - x(t) \quad (\text{A.2})$$

where  $x_0$  is the setpoint and  $x(t)$  the signal measured by the DAQ. This error signal is then corrected to give an output signal  $u(t)$ :

$$u(t) = K_p e(t) + K_i \int_0^t e(\tau) d\tau + K_d \frac{de(t)}{dt} \quad (\text{A.3})$$

where  $K_p$ ,  $K_i$  and  $K_d \propto -\Gamma^{cool}$  are respectively the proportional, integral and derivative gain coefficients of a feedback loop.

As the proportional feedback is directly proportional to the error on the position of the sphere, adjusting the value of  $K_p$  means modulating the stiffness of the trap (see Equation 1.11). On the other hand, the integral term sums the accumulated errors of the sphere's position over time and thus enables corrections of drifts that cannot be corrected by the proportional feedback alone. In the feedback system of this setup, both three gains are used, except the proportional gain in the radial X and Y directions for which a smoother trap is desired to allow greater displacements of the sphere in these directions.

In practice, a PID controller can be implemented using frequency-tuneable electronic filters. More specifically, the derivative damping part of the feedback can be realized through a high-pass filter, which cut-off frequency is set above the resonance frequency of the sphere such as to damp its resonance motion while weakly acting below the resonance frequency where final gravity measurements are to be performed.



## Appendix B

# Spectral Analysis

The motion of the sphere is analysed in the frequency domain. The following analysis holds for all three directions of space. If one of the position timestreams  $x(t)$  is acquired during  $T_{acq}$ , its power spectral density (PSD)  $S_{xx}(\omega)$  is defined as:

$$S_{xx}(\omega) = \frac{1}{T_{acq}} |\hat{x}(\omega)|^2 \quad (\text{B.1})$$

where  $\hat{x}(f)$  is the Fourier transformations of  $x(t)$ :

$$\hat{x}(\omega) = \int_{-T_{acq}/2}^{T_{acq}/2} e^{i\omega t} x(t) dt \quad (\text{B.2})$$

As the average power of  $x(t)$  during  $T_{acq}$  is given by (where the second equality is derived from Parseval's theorem for a signal with finite total energy):

$$P_{av} = \frac{1}{\sqrt{T_{acq}}} \int_{-T_{acq}/2}^{T_{acq}/2} |x(t)|^2 dt = \frac{1}{\sqrt{T_{acq}}} \int |\hat{x}(\omega)|^2 d\omega \quad (\text{B.3})$$

$S_{xx}(\omega)$  is a density function characterizing the average power carried by  $x(t)$  for a given frequency. In other words, the power spectral density of a signal informs us about the distribution of a given signal's average power during a given acquisition time in the frequency domain. It is thus expressed in  $V^2/Hz$ . Integrating  $S_{xx}(\omega)$  over all frequencies gives the average power of the overall signal.

Another commonly-used variable is the amplitude spectral density of  $x(t)$ ,  $\sqrt{S(\omega)}$ , defined as the square root of the power spectral density (expressed in  $V/\sqrt{Hz}$ ):

$$\sqrt{S_{xx}(\omega)} = \frac{1}{\sqrt{T_{acq}}} |\hat{x}(\omega)| \quad (\text{B.4})$$



## Appendix C

# Calculation of the Yukawa potential for this experiment

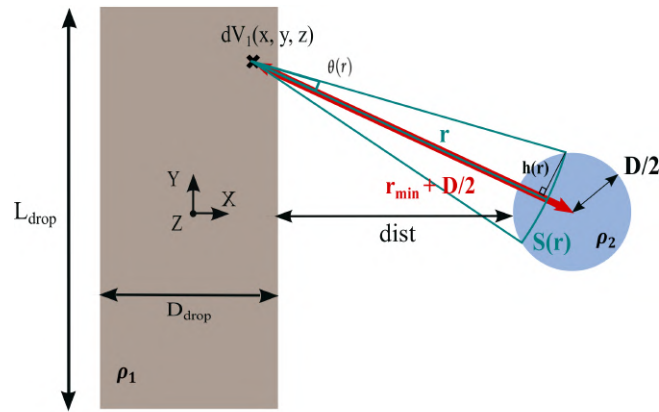


FIGURE C.1: Geometry of one droplet and the sphere in the X-Y plane. The origin is set at the center of the cylindrical droplet. The walls of the capillary are not considered here. We evaluate the Yukawa potential between an infinitesimal volume  $dV_1(x, y, z)$  in the droplet and the whole sphere. The minimum distance between  $dV_1(x, y, z)$  and the surface of the sphere with diameter  $D$  is  $r_{min}$ . The integration over the volume of the sphere is performed through successive spherical caps with radius  $r$ , centered on  $dV_1(x, y, z)$ .

The Yukawa infinitesimal potential  $dU_{12}$  between a point mass  $dm_1$  in the droplet and a point mass  $dm_2$  in the sphere separated by distance  $r$  can be written as:

$$dU_{12} = -\frac{Gdm_1dm_2}{r} \left(1 + \alpha e^{-\frac{r}{\lambda}}\right) \quad (\text{C.1})$$

where  $G$  is the gravitational constant. Knowing the mass density  $\rho_1$  of the droplet and the mass density  $\rho_2$  of the sphere, the expressions of the point masses are:

$$dm_1 = \rho_1 dV_1 \quad \text{and} \quad dm_2 = \rho_2 dV_2 \quad (\text{C.2})$$

where  $dV_1$  and  $dV_2$  are the associated infinitesimal volumes. Therefore, if  $r_{min}$  is the minimum distance between an infinitesimal volume  $dV_1$  in the droplet and the the surface of the sphere (see Figure C.1), the Yukawa potential between them can be obtained by an integration over the volume of the sphere:

$$dU_1(r_{min}) = -G\rho_1\rho_2dV_1 \int_{r_{min}}^{r_{min}+D} \frac{S(r)}{r} \left(1 + \alpha e^{-\frac{r}{\lambda}}\right) dr \quad (\text{C.3})$$

where  $S(r)$  is the area of a spherical cap with radius  $r$  and polar angle  $\theta(r)$  (see Figure C.1):

$$S(r) = 2\pi r [1 - \cos \theta(r)] \quad (C.4)$$

$$\theta(r) = \arcsin \left( \frac{h(r)}{r} \right) \quad (C.5)$$

where the expression of the height  $h(r)$  is given by:

$$h(r) = \frac{1}{2(r_{min} + \frac{D}{2})} \left\{ 4 \left( r_{min} + \frac{D}{2} \right)^2 r^2 - \left[ \left( r_{min} + \frac{D}{2} \right)^2 - \left( \frac{D}{2} \right)^2 + r^2 \right] \right\}^{1/2} \quad (C.6)$$

Hence the final expression of the Yukawa potential between the sphere and an infinitesimal volume  $dV_1$  of the droplet:

$$\begin{aligned} dU_1(r_{min}) &= -G\rho_1\rho_2 dV_1 \times \int_{r_{min}}^{r_{min}+D} 2\pi r \left\{ 1 - \cos \left[ \arcsin \left( \frac{h(r)}{r} \right) \right] \right\} \left( \frac{1 + \alpha e^{-\frac{r}{\lambda}}}{r} \right) dr \\ &= -G\rho_1\rho_2 dV_1 \times f(r_{min}, \alpha, \lambda) \end{aligned} \quad (C.7)$$

The analytical result of  $f(r_{min}, \alpha, \lambda)$  is:

$$f(r_{min}, \alpha, \lambda) = \frac{2\pi\alpha\lambda^2 (d + 2\lambda + (d - 2\lambda)e^{d/\lambda}) e^{-\frac{d+r_{min}}{\lambda}}}{d + 2r_{min}} \quad (C.8)$$

The associated Yukawa force is defined by:

$$dF_1(r_{min}) = -\frac{dU_1}{dr_{min}}(r_{min}) \quad (C.9)$$

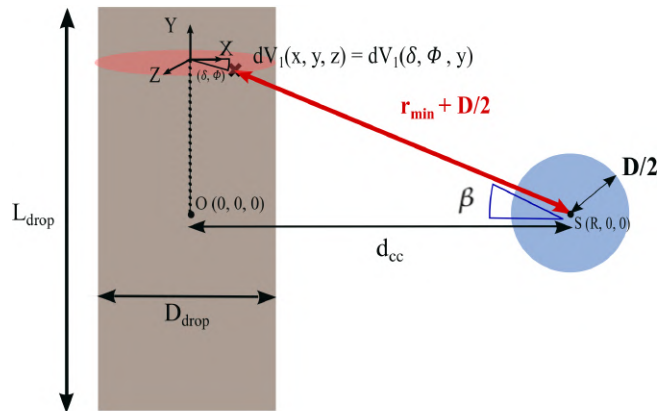


FIGURE C.2: Geometry of one droplet and the sphere showing the cylindrical coordinates of  $dV_1(x, y, z) = dV_1(\delta \cos \Phi, y, \delta \sin \Phi)$ .  $\beta$  is the angle between  $\vec{S}_{sph}O$  and  $\vec{S}_{sph}dV_1$ .

In order to integrate the Yukawa force over the whole droplet, we use the cylindrical coordinates of the infinitesimal volume  $dV_1$ :

$$dV_1(x, y, z) = dV_1(\delta \cos \Phi, y, \delta \sin \Phi) \quad (\text{C.10})$$

where  $(x, z) = (\delta \cos \Phi, \delta \sin \Phi)$  are the polar coordinates of  $dV_1$  in the X-Z plane (see Figure C.2). If we call  $d_{cc} = \frac{D_{drop}}{2} + dist + \frac{D}{2}$ , we have:

$$r_{min}(\delta, \Phi, y) = -\frac{D}{2} + (d_{cc}^2 + y^2 + \delta^2 - 2R\delta \cos \Phi) \quad (\text{C.11})$$

As only the projection of  $dF_1(r_{min})$  on the X-axis will add to a non zero after integration due to symmetry arguments, we only consider the projection  $dF_{x1}(r_{min})$  of  $dF_1(r_{min})$  on the X-axis:

$$dF_{x1}(r_{min}) = dF_1(r_{min}) \cos \beta \quad (\text{C.12})$$

where  $\beta$  is the angle between  $\overrightarrow{S_{sph}\vec{O}}$  and  $\overrightarrow{S_{sph}dV_1}$  (see Figure C.2):

$$\beta(r_{min}) = \arcsin \left( \frac{\sqrt{(\delta \sin \Phi)^2 + y^2}}{r_{min} + \frac{D}{2}} \right) \quad (\text{C.13})$$

The total Yukawa force can thus be derivated as follows:

$$F_x = \int_{y=-\frac{L_{drop}}{2}}^{\frac{L_{drop}}{2}} \int_{\Phi=0}^{2\pi} \int_{\delta=0}^{\frac{D_{drop}}{2}} dF_1(r_{min}(\delta, \Phi, y)) \cos \beta \delta d\delta d\Phi dy \quad (\text{C.14})$$

These final calculations were performed using Python and can be adapted when adding the walls of the capillary, varying the ID and OD of the capillary, the distance between the droplet and the sphere, the mass density of the droplet or the center position of the droplet.



# Bibliography

- [1] D. J. Griffiths, *Introduction to elementary particles*. John Wiley Sons, Inc, 1987.
- [2] A. Zee, *Quantum field in a nutshell*. Princeton, 2010.
- [3] N. Arkani-Hamed, S. Dimopoulos, and G. Dvali, “The hierarchy problem and new dimensions at a millimeter”, *Physics Letters B*, vol. 429, no. 3, pp. 263 – 272, 1998, ISSN: 0370-2693. DOI: [https://doi.org/10.1016/S0370-2693\(98\)00466-3](https://doi.org/10.1016/S0370-2693(98)00466-3). [Online]. Available: <http://www.sciencedirect.com/science/article/pii/S0370269398004663>.
- [4] N. Arkani-Hamed, S. Dimopoulos, and G. Dvali, “Phenomenology, astrophysics, and cosmology of theories with submillimeter dimensions and TeV scale quantum gravity”, *Phys. Rev. D*, vol. 59, no. 8, p. 086004, Mar. 1999. DOI: [10.1103/PhysRevD.59.086004](https://doi.org/10.1103/PhysRevD.59.086004). [Online]. Available: <https://link.aps.org/doi/10.1103/PhysRevD.59.086004>.
- [5] I. Antoniadis, S. Dimopoulos, and G. Dvali, “Millimetre-range forces in superstring theories with weak-scale compactification”, *Nuclear Physics B*, vol. 516, no. 1, pp. 70 –82, 1998, ISSN: 0550-3213. DOI: [https://doi.org/10.1016/S0550-3213\(97\)00808-0](https://doi.org/10.1016/S0550-3213(97)00808-0). [Online]. Available: <http://www.sciencedirect.com/science/article/pii/S0550321397008080>.
- [6] I. Antoniadis, N. Arkani-Hamed, S. Dimopoulos, and G. Dvali, “New dimensions at a millimeter to a fermi and superstrings at a TeV”, *Physics Letters B*, vol. 436, no. 3, pp. 257 –263, 1998, ISSN: 0370-2693. DOI: [https://doi.org/10.1016/S0370-2693\(98\)00860-0](https://doi.org/10.1016/S0370-2693(98)00860-0). [Online]. Available: <http://www.sciencedirect.com/science/article/pii/S0370269398008600>.
- [7] S. Dimopoulos and G. F. Giudice, “Macroscopic forces from supersymmetry”, *Physics Letters B*, vol. 379, no. 1, pp. 105 –114, 1996, ISSN: 0370-2693. DOI: [https://doi.org/10.1016/0370-2693\(96\)00390-5](https://doi.org/10.1016/0370-2693(96)00390-5). [Online]. Available: <http://www.sciencedirect.com/science/article/pii/0370269396003905>.
- [8] E. Adelberger, B. Heckel, and A. Nelson, “TESTS OF THE GRAVITATIONAL INVERSE-SQUARE LAW”, *Annual Review of Nuclear and Particle Science*, vol. 53, no. 1, pp. 77–121, 2003. DOI: [10.1146/annurev.nucl.53.041002.110503](https://doi.org/10.1146/annurev.nucl.53.041002.110503). [Online]. Available: <https://doi.org/10.1146/annurev.nucl.53.041002.110503>.
- [9] J. Murata and S. Tanaka, “Review of short-range gravity experiments in the LHC era”, *Classical and Quantum Gravity*, vol. 32, 2014. DOI: [10.1088/0264-9381/32/3/033001](https://doi.org/10.1088/0264-9381/32/3/033001).
- [10] S. M. Merkowitz, “Tests of gravity using lunar laser ranging”, *Living Reviews in Relativity*, vol. 13, no. 1, p. 7, Nov. 2010, ISSN: 1433-8351. DOI: [10.12942/lrr-2010-7](https://doi.org/10.12942/lrr-2010-7). [Online]. Available: <https://doi.org/10.12942/lrr-2010-7>.

- [11] D Borka, P. Jovanović, V. Borka Jovanović, and A. Zakharov, “Constraining the range of yukawa gravity interaction from s2 star orbits”, *Journal of Cosmology and Astroparticle Physics*, vol. 11, pp. 050–1, 2013. DOI: [10.1088/1475-7516/2013/11/050](https://doi.org/10.1088/1475-7516/2013/11/050).
- [12] D. C. Moore, “Tests of fundamental physics with optically levitated microspheres in high vacuum”, 2018, p. 18. DOI: [10.1117/12.2322829](https://doi.org/10.1117/12.2322829).
- [13] Y.-J. Chen, W. K. Tham, D. E. Krause, D. López, E. Fischbach, and R. S. Decca, “Stronger limits on hypothetical yukawa interactions in the 30–8000 nm range”, *Phys. Rev. Lett.*, vol. 116, p. 221 102, 22 2016. DOI: [10.1103/PhysRevLett.116.221102](https://doi.org/10.1103/PhysRevLett.116.221102). [Online]. Available: <https://link.aps.org/doi/10.1103/PhysRevLett.116.221102>.
- [14] *Henry cavendish (1731–1810): Experiments to determine the density of the earth, a source book in geology, 1400–1900*.
- [15] D. J. Kapner, T. S. Cook, E. G. Adelberger, J. H. Gundlach, B. R. Heckel, C. D. Hoyle, and H. E. Swanson, “Tests of the gravitational inverse-square law below the dark-energy length scale”, *Phys. Rev. Lett.*, vol. 98, no. 2, p. 021 101, Jan. 2007. DOI: [10.1103/PhysRevLett.98.021101](https://doi.org/10.1103/PhysRevLett.98.021101). [Online]. Available: <https://link.aps.org/doi/10.1103/PhysRevLett.98.021101>.
- [16] A. A. Geraci, S. J. Smullin, D. M. Weld, J. Chiaverini, and A. Kapitulnik, “Improved constraints on non-newtonian forces at 10 microns”, *Phys. Rev. D*, vol. 78, no. 2, p. 022 002, Jul. 2008. DOI: [10.1103/PhysRevD.78.022002](https://doi.org/10.1103/PhysRevD.78.022002). [Online]. Available: <https://link.aps.org/doi/10.1103/PhysRevD.78.022002>.
- [17] G. V. Philip H. Jones M. Maragò, *Optical tweezers principles and applications*. Cambridge University Press, February 2016.
- [18] A. Ashkin, “Trapping of atoms by resonance radiation pressure”, *Phys. Rev. Lett.*, vol. 40, pp. 729–732, 12 1978. DOI: [10.1103/PhysRevLett.40.729](https://doi.org/10.1103/PhysRevLett.40.729). [Online]. Available: <https://link.aps.org/doi/10.1103/PhysRevLett.40.729>.
- [19] A. Ashkin and J. M. Dziedzic, “Optical levitation in high vacuum”, *Applied Physics Letters*, vol. 28, no. 6, pp. 333–335, 1976. DOI: [10.1063/1.88748](https://doi.org/10.1063/1.88748). eprint: <https://doi.org/10.1063/1.88748>. [Online]. Available: <https://doi.org/10.1063/1.88748>.
- [20] ———, “Feedback stabilization of optically levitated particles”, *Applied Physics Letters*, vol. 30, no. 4, pp. 202–204, 1977. DOI: [10.1063/1.89335](https://doi.org/10.1063/1.89335). eprint: <https://doi.org/10.1063/1.89335>. [Online]. Available: <https://doi.org/10.1063/1.89335>.
- [21] ———, “Stability of optical levitation by radiation pressure”, *Applied Physics Letters*, vol. 24, no. 12, pp. 586–588, 1974. DOI: [10.1063/1.1655064](https://doi.org/10.1063/1.1655064). eprint: <https://doi.org/10.1063/1.1655064>. [Online]. Available: <https://doi.org/10.1063/1.1655064>.
- [22] A. Ashkin, J. M. Dziedzic, and T. Yamane, “Optical trapping and manipulation of single cells using infrared laser beams”, *Nature*, vol. 330, no. 6150, pp. 769–771, Dec. 1, 1987, ISSN: 1476-4687. DOI: [10.1038/330769a0](https://doi.org/10.1038/330769a0). [Online]. Available: <https://doi.org/10.1038/330769a0>.
- [23] A Ashkin and J. Dziedzic, “Optical trapping and manipulation of viruses and bacteria”, *Science*, vol. 235, no. 4795, pp. 1517–1520, 1987, ISSN: 0036-8075. DOI: [10.1126/science.3547653](https://doi.org/10.1126/science.3547653). [Online]. Available: <https://science.sciencemag.org/content/235/4795/1517>.

- [24] K. C. Neuman and S. M. Block, "Optical trapping", *Review of Scientific Instruments*, vol. 75, no. 9, pp. 2787–2809, 2004. DOI: [10.1063/1.1785844](https://doi.org/10.1063/1.1785844). [Online]. Available: <https://doi.org/10.1063/1.1785844>.
- [25] D. C. Moore, A. D. Rider, and G. Gratta, "Search for millicharged particles using optically levitated microspheres", *Phys. Rev. Lett.*, vol. 113, p. 251 801, 25 2014. DOI: [10.1103/PhysRevLett.113.251801](https://doi.org/10.1103/PhysRevLett.113.251801). [Online]. Available: <https://link.aps.org/doi/10.1103/PhysRevLett.113.251801>.
- [26] A. A. Geraci, S. B. Papp, and J. Kitching, "Short-range force detection using optically cooled levitated microspheres", *Phys. Rev. Lett.*, vol. 105, p. 101 101, 10 2010. DOI: [10.1103/PhysRevLett.105.101101](https://doi.org/10.1103/PhysRevLett.105.101101). [Online]. Available: <https://link.aps.org/doi/10.1103/PhysRevLett.105.101101>.
- [27] A. D. Rider, D. C. Moore, C. P. Blakemore, M. Louis, M. Lu, and G. Gratta, "Search for screened interactions associated with dark energy below the 100  $\mu\text{m}$  length scale", *Phys. Rev. Lett.*, vol. 117, p. 101 101, 10 2016. DOI: [10.1103/PhysRevLett.117.101101](https://doi.org/10.1103/PhysRevLett.117.101101). [Online]. Available: <https://link.aps.org/doi/10.1103/PhysRevLett.117.101101>.
- [28] A. Ashkin, "Acceleration and trapping of particles by radiation pressure", *Phys. Rev. Lett.*, vol. 24, no. 4, pp. 156–159, Jan. 1970. DOI: [10.1103/PhysRevLett.24.156](https://doi.org/10.1103/PhysRevLett.24.156). [Online]. Available: <https://link.aps.org/doi/10.1103/PhysRevLett.24.156>.
- [29] A. Ashkin, J. Dziedzic, J. Bjorkholm, and S. Chu, "Observation of a single-beam gradient force optical trap for dielectric particles", in *Optical Angular Momentum*, 2016, pp. 196–198.
- [30] A. Ashkin, "Forces of a single-beam gradient laser trap on a dielectric sphere in the ray optics regime", *Biophysical Journal*, vol. 61, no. 2, pp. 569–582, 1992, ISSN: 0006-3495. DOI: [https://doi.org/10.1016/S0006-3495\(92\)81860-X](https://doi.org/10.1016/S0006-3495(92)81860-X). [Online]. Available: <http://www.sciencedirect.com/science/article/pii/S000634959281860X>.
- [31] D. S. Lemons and A. Gythiel, "Paul langevin's 1908 paper "on the theory of brownian motion" ["sur la théorie du mouvement brownien," c. r. acad. sci. (paris) 146, 530–533 (1908)]", *American Journal of Physics*, vol. 65, no. 11, pp. 1079–1081, 1997. DOI: [10.1119/1.18725](https://doi.org/10.1119/1.18725). [Online]. Available: <https://doi.org/10.1119/1.18725>.
- [32] F. Monteiro, S. Ghosh, A. G. Fine, and D. C. Moore, "Optical levitation of 10-ng spheres with nano-g acceleration sensitivity", *Phys. Rev. A*, vol. 96, p. 063 841, 6 2017. DOI: [10.1103/PhysRevA.96.063841](https://doi.org/10.1103/PhysRevA.96.063841). [Online]. Available: <https://link.aps.org/doi/10.1103/PhysRevA.96.063841>.
- [33] T. Li, "Fundamental tests of physics with optically trapped microspheres", 216 pages, PhD thesis, THE UNIVERSITY OF TEXAS AT AUSTIN, 2011.
- [34] P. Kwee, F. Seifert, B. Willke, and K. Danzmann, "Laser beam quality and pointing measurement with an optical resonator", *Review of Scientific Instruments*, vol. 78, no. 7, p. 073 103, 2007. DOI: [10.1063/1.2754400](https://doi.org/10.1063/1.2754400). eprint: <https://doi.org/10.1063/1.2754400>. [Online]. Available: <https://doi.org/10.1063/1.2754400>.

- [35] A. D. Rider, D. C. Moore, C. P. Blakemore, M. Louis, M. Lu, and G. Gratta, "Search for screened interactions associated with dark energy below the 100  $\mu\text{m}$  length scale", *Phys. Rev. Lett.*, vol. 117, p. 101 101, 10 2016. DOI: [10 . 1103 / PhysRevLett . 117 . 101101](https://doi.org/10.1103/PhysRevLett.117.101101). [Online]. Available: <https://link.aps.org/doi/10.1103/PhysRevLett.117.101101>.
- [36] F. Monteiro, S. Ghosh, E. C. van Assendelft, and D. C. Moore, "Optical rotation of levitated spheres in high vacuum", *Phys. Rev. A*, vol. 97, p. 051 802, 5 2018. DOI: [10 . 1103 / PhysRevA . 97 . 051802](https://doi.org/10.1103/PhysRevA.97.051802). [Online]. Available: <https://link.aps.org/doi/10.1103/PhysRevA.97.051802>.
- [37] *Face seal o-ring gland width and depth default recomendations*. [Online]. Available: <https://www.marcorubber.com/o-ring-groove-design-face-seal.htm>.
- [38] A. O. Sushkov, W. J. Kim, D. A. R. Dalvit, and S. K. Lamoreaux, "New experimental limits on non-newtonian forces in the micrometer range", *Phys. Rev. Lett.*, vol. 107, no. 17, p. 171 101, Oct. 2011. DOI: [10 . 1103 / PhysRevLett . 107 . 171101](https://doi.org/10.1103/PhysRevLett.107.171101). [Online]. Available: <https://link.aps.org/doi/10.1103/PhysRevLett.107.171101>.
- [39] W. J. Kim, A. O. Sushkov, D. A. R. Dalvit, and S. K. Lamoreaux, "Surface contact potential patches and casimir force measurements", *Phys. Rev. A*, vol. 81, no. 2, p. 022 505, Feb. 2010. DOI: [10 . 1103 / PhysRevA . 81 . 022505](https://doi.org/10.1103/PhysRevA.81.022505). [Online]. Available: <https://link.aps.org/doi/10.1103/PhysRevA.81.022505>.
- [40] A. D. Rider, "Measurements with optically levitated microspheres", 153 pages, PhD thesis, Stanford University, 2019.